

New insights into the delayed initiation of a debris flow in southwest China

Taixin Peng

Institute of Mountain Hazards and Environment Chinese Academy of Sciences

N. Sh. Chen (✉ chennsh@imde.ac.cn)

Institute of Mountain Hazards and Environment <https://orcid.org/0000-0002-6135-0739>

Guisheng Hu

Institute of Mountain Hazards and Environment Chinese Academy of Sciences

Shufeng Tian

Institute of Mountain Hazards and Environment Chinese Academy of Sciences

Zheng Han

Central South University

Enlong Liu

Sichuan University

Research Article

Keywords: delayed debris flow, hollow deposits, landslide initiation, fluid-solid coupling

Posted Date: February 23rd, 2021

DOI: <https://doi.org/10.21203/rs.3.rs-221141/v1>

License:   This work is licensed under a Creative Commons Attribution 4.0 International License.

[Read Full License](#)

1 **New insights into the delayed initiation of a debris flow in**

2 **southwest China**

3 Taixin Peng^{1,2}, Ningsheng Chen^{1,3,*}, Guisheng Hu^{1,3}, Shufeng Tian^{1,2}, Zheng Han⁴, Enlong
4 Liu⁵

5 **Corresponding author. Ningsheng Chen (chennsh@imde.ac.cn.)**

6 1 Key Lab of Mountain Hazards and Surface Process, Institute of Mountain Hazards and
7 Environment (IMHE), Chinese Academy of Sciences, Chengdu 610041, China.

8 2 University of Chinese Academy of Sciences, Beijing 100049, China.

9 3 Academy of Plateau Science and Sustainability, Xining 810016, P.R.China.

10 4 School of Civil Engineering, Central South University, Changsha, 410075, China.

11 5 State Key Laboratory of Hydraulics and Mountain River Engineering, College of Water
12 Resources and Hydropower, Sichuan University, Chengdu 610065, China.

13 **Abstract.**¹ On 6 July 2020, 3 h 40 min after rainfall stopped, a delayed debris-flow disaster
14 occurred due to colluvium deposits in a hollow region (CDH) in the Chenghuangmiao gully,
15 Sichuan Province, China, which resulted in 4 deaths and 27 injuries. This study explores the

¹ **Abbreviations**

CDH: colluvium deposits in a hollow region; SCS: US Soil Conservation Service

16 initiation process of the delayed debris flow and the cause for the delay. Field investigations,
17 catchment geometry interpretation, laboratory tests, theoretical calculations, and fluid-solid
18 coupling numerical simulation were performed to obtain landslide parameters and understand
19 the mechanisms of the event. Results show: (1) The event was a giant low-frequency viscous
20 debris flow. (2) Its initiation was caused by the delayed landslide process under the influence
21 of back-end confluence. (3) The debris-flow discharge in the main gully increased over 19.5
22 min. (4) The seepage process inside the CDH continued for 3 h 20 min after the rainfall
23 stopped before its pore pressure and reduction in strength was sufficient to initiate the debris
24 flow. This research provides new insights on delayed debris-flow disasters; it is a reference
25 for improving disaster management systems, especially monitoring and early warning
26 systems, thereby avoiding future casualties.

27 **Keywords:** delayed debris flow; hollow deposits; landslide initiation; fluid-solid coupling

28 **1 Introduction**

29 Debris flows are triggered by high-intensity and short-duration, or low-intensity and long-
30 duration rainfall (Iverson 1997; Iverson et al. 1997). When rainfall intensity and duration
31 reach critical levels, debris flow occurs (Baum and Godt 2010; Cannon et al. 2011; Cannon et
32 al. 2008; Guzzetti et al. 2008). Therefore, China's Sichuan Province has established many
33 rainfall stations to monitor likely occurrences of debris flow in vulnerable areas and warn
34 people about them. During 2019–2020, warnings for 14 debris flows were successfully issued,

35 preventing 4932 casualties. However, this early warning mechanism is not perfect as delays
36 make the warnings ineffective. The Chenghuangmiao Gully experienced heavy rainfall in
37 Aba, Sichuan on 5 July, 2020. People were evacuated when the alarm sounded, and they
38 returned when the rain stopped; however, the debris-flow disaster initiated by the colluvium
39 deposits in a hollow region (CDH) occurred 3 h 40 min after the rainfall stopped, causing 4
40 deaths. Accordingly, the following questions must be addressed: How was this delayed debris
41 flow initiated? What caused the delay?

42 Delays in the occurrence of landslides after rainfall is a common phenomenon. Because they
43 may take a long time to develop. The development of landslides has three stages: initial,
44 secondary, and accelerated deformation. Statistical data on 20 large-scale landslides show
45 that the three stages together take 21 to 2135 days ([Deng et al. 2000](#); [Huang et al. 2012](#); [Lee
46 et al. 2014](#); [Li et al. 2016](#); [Qi et al. 2006](#); [Qiang et al. 2008](#)). As the delay in the development
47 of a landslide occurs, delay in the resultant debris flow is possible. Analyses through
48 numerous cases studies and experiments have explained the initiation mechanism of debris
49 flow triggered by landslides. High pore pressure causes softening or liquefaction of the soil to
50 initiate debris flow; however, researchers have suggested that the processes involved in this
51 type of debris flow must be studied further ([Crosta and Dal Negro 2003](#); [Feng et al. 2005](#);
52 [Iverson and Denlinger 2001](#); [Iverson and Vallance 2001](#)). The debris-flow disaster initiated
53 by the CDH landslide resulted from processes such as rainfall generation and confluence of

54 streams, landslide, and debris flow (Chen et al. 2007; Zhang et al. 2019). As these three
55 processes occur over various durations, they must be studied individually. The following
56 approaches are relevant:

57 1) Rainfall generation and confluence: The US Soil Conservation Service (SCS) model and
58 the rational formula model are universally recognised and are also used in China. These
59 methods involve calculating the total surface runoff, the runoff generation time, and the peak
60 flow of confluence by combining rational formulas with regional experience coefficients
61 (Alfieri et al. 2008; Hua et al. 2003; Mishra and Singh 2003; Yue et al. 2012). 2) The CDH
62 landslide: Seepage and deformation occurred in the CDH simultaneously under the influence
63 of back-end confluence; their interaction (fluid–solid coupling) can be simulated using the
64 finite-difference software (Kim et al. 2018; Singh et al. 2008; Zhou et al. 2019). 3) Debris
65 flow: Calculation of velocity and discharge of debris flow based on cross-section
66 investigation; this method is widely used for preliminary evaluation of debris flow and
67 engineering treatment (Chen et al. 2015).

68 In general, from the onset of rainfall to the occurrence of debris flow, there were mature
69 studies on back end confluence, seepage and deformation of the landslide, and debris flow
70 respectively. However, the disaster's physical process was not connected in series on the
71 timeline as real happened. The phenomenon of debris flow delay is mentioned in literature
72 but has not been researched adequately. In this study, we use the SCS model and the rational

73 formula to calculate the back-end confluence of the CDH; we then use a numerical method to
74 simulate the debris flow initiated by the CDH landslide in the conditions of the back-end
75 confluence. Through field investigation, catchment geometry interpretation, and laboratory
76 tests the debris flow was characterized. Consequently, we identified the process of debris
77 flow initiation and the reasons for the delay in its onset.

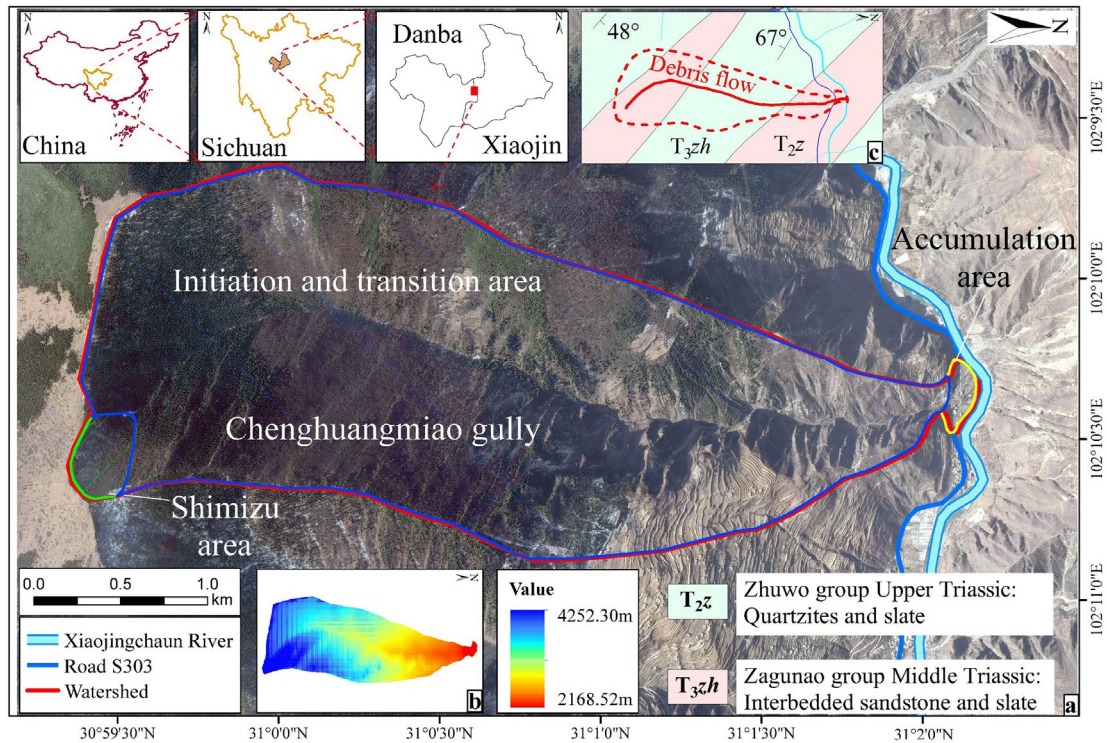
78 **2 Study area**

79 **2.1 Overview of geography, geology, and watershed of the catchment**

80 The study area is located at the junction of Xiaojin County and Danba County in Sichuan
81 Province, China, at a valley on the southeast edge of the Qinghai–Tibet Plateau. The region
82 comprises middle mountain landforms that exhibit rapid structural uplift, deep river cutting,
83 and intense erosion and weathering (Fig. 1a). The study area is situated in the western wing
84 of the Xiaojin Arc structure, which comprises two anticlines that sandwich a syncline; the
85 three folds are aligned along the N–SW direction. The Chenghuangmiao Gully flows between
86 the cores of the two anticlines (Fig. 1c). The lithology of the study area comprises slates,
87 quartzites, and interbedded sandstones (Fig. 1c).

88 The watershed where the debris flow erupted belongs to a branch of the Xiaojinchuan River
89 at the Chenghuangmiao Gully. The watershed area is 6.1 km², altitude is between 2168 m and
90 4252 m, and relief of the basin is 2084 m. The Xiaojinchuan River and the Provincial
91 Highway S303 pass through the mouth of the gully. Based on the longitudinal gradient and

92 source distribution of the Chenghuangmiao Gully, the watershed is divided into the
93 confluence area (Shimizu area) at the back end of the CDH, initiation and transition area, and
94 accumulation area. The Shimizu area is located in the upper reaches of the Chenghuangmiao
95 Gully above the altitude of 4060 m, with an area of 0.123 km² and a slope of 26–38°. The
96 vegetation in the area is developed and the humus layer and colluvium deposits are 0.9–2.3 m
97 thick. The concave terrain at the junction of the two watersheds provides favourable
98 conditions for runoff confluence at the back end of the CDH. The altitudes of the initiation
99 and transition areas are between 4060 m and 2250 m, length is approximately 4.95 km, and
100 area is approximately 5.930 km². Abundant loose materials and steep gradient channels
101 provide favourable conditions for the initiation and transition of debris flows. The
102 accumulation area is located from the mouth of the Chenghuangmiao Gully (2250 m in
103 elevation) to the confluence point with the Xiaojinchuan river (2168 m in elevation) and the
104 area is approximately 0.047 km². The relatively low slope provides good topographical
105 conditions for the accumulation of debris (Fig. 1a and b).



106

107

Fig. 1. Chenghuangmiao Gully: (a) watershed; (b) altitude; (c) geological map.

108

2.2 Weather overview

109

The study area experienced sparse rainfall in spring and heavy rainfall in June; intermittent

110

heavy rainfall occurred before the debris flow event. According to statistics, the maximum

111

monthly precipitation in the study area since 1952 was 233.9 mm, and the precipitation in

112

June 2020 (222.6 mm), before the occurrence of the debris flow, was close to the historical

113

peak (Fig. 2a and b). The maximum daily rainfall of 30 mm/d occurred on the day before the

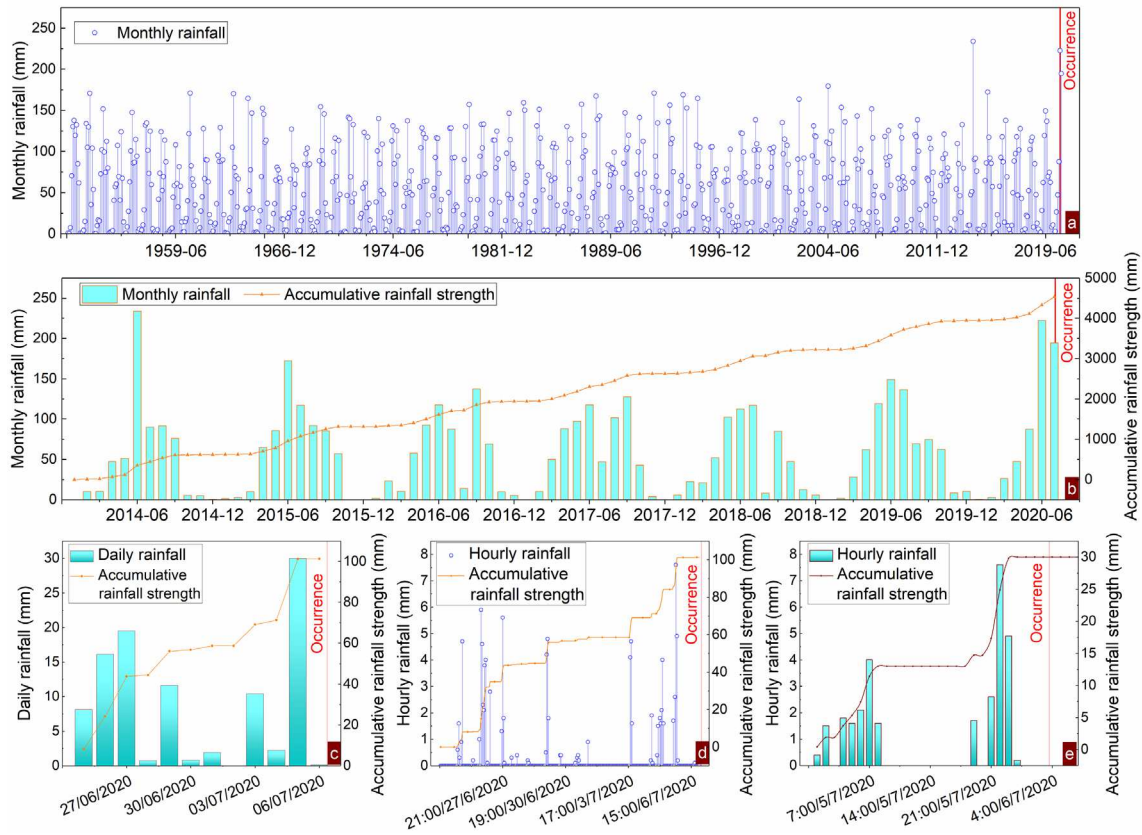
114

occurrence of the debris flow (5 July 2020); this value was close to the historical maximum

115

daily rainfall of 37.8 mm/d (Fig. 2c). The maximum hourly rainfall was 7.6 mm/h from 21:00

116 to 22:00 h on 5 July 2020 (Fig. 2d). The data show that rainfall occurred throughout the area
 117 during 01:00–08:00 h and 19:00–24:00 h on 5 July 2020. The effective rainfall was
 118 approximately 17.0 mm before the disaster (Fig. 2e).

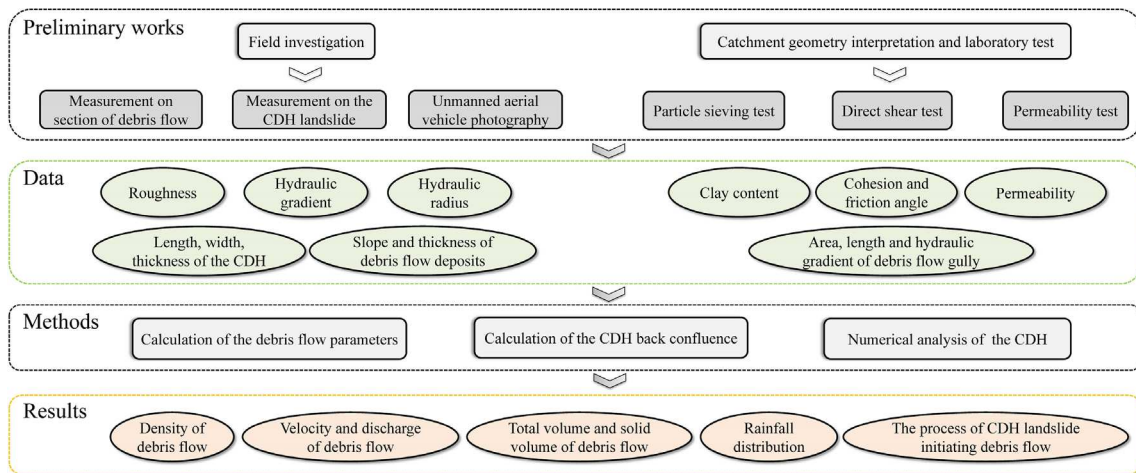


119

120 **Fig. 2.** Rainfall trends in the study area: (a) Monthly rainfall from 1952; (b) Monthly rainfall
 121 from 2014 to 2020; (c) Daily rainfall in the 12 days before the occurrence of debris flow; (d)
 122 Hourly rainfall in the 12 days before the occurrence; (e) Hourly rainfall 30 h before the
 123 occurrence.

124 **3 Methodology**

125 Field investigations, catchment geometry interpretation, and laboratory tests were conducted
126 to obtain data on deposits and terrain parameters for the characterisation of the gully after the
127 debris-flow disaster. Theoretical calculations and numerical simulation methods were
128 performed to obtain the parameters regarding rainfall, runoff, CDH landslide at the debris-
129 flow source, and debris flow (Fig. 3).



130

131

Fig. 3. Methodology used to analyse the initiation of debris flow.

132 **3.1 Field investigations, catchment geometry interpretation, and laboratory tests**

133 Field investigations were performed to ascertain the following: 1) Terrain parameters of the
134 debris flow accumulation body were evaluated through sampling at the gully mouth and
135 aerial photography using an unmanned aerial vehicle. 2) The geometric parameters of the
136 gully section such as maximum mud-mark height and widths of the section at the top and

137 bottom. 3) Terrain parameters and the composition of the CDH landslide at the source of
138 debris flow.

139 Catchment geometry was interpreted to obtain its terrain parameters such as watershed area,
140 gully length of debris flow, and hydraulic gradient. Laboratory tests, such as particle sieve
141 analysis (Malvern), direct shear test, and permeability test, were conducted on the
142 accumulated deposits of less than 60 mm accumulated in the area. In addition, physical and
143 mechanical parameters of the deposits were obtained.

144 **3.2 Calculation of back-end confluence process**

145 We obtained the surface-runoff at the confluence outlet through calculations using the SCS
146 model, rational formula, and the pentagonal flow-process line method. First, the SCS model
147 was used to calculate total surface runoff. The rational formula was used to calculate hourly
148 peak-flow rate and runoff-generation time. Based on these calculations, the pentagon-flow
149 process line per hour was superimposed, and we obtained the surface-runoff process line
150 (Clark 1945; Edward Kuiper C.I. 1965; Pegram and Parak 2004). Finally, we obtained the
151 subsurface-runoff process line according to the empirical method and formed a complete-
152 runoff process line for the confluence to the CDH.

153 The SCS model is composed of three relational equations: the equation for rainfall and runoff,
154 the water balance equation, the linear equations of initial rainfall loss. The above three
155 relational equations are combined to obtain the equations of the SCS model (Eqs. (1) and (2)).

$$156 \quad S = \frac{25400}{CN} - 254 \quad (1)$$

$$157 \quad \left. \begin{aligned} Q &= (P - 0.2S)^2 / (P + 0.8S), P \geq 0.2S \\ Q &= 0, P < 0.2S \end{aligned} \right\} \quad (2)$$

158 where P refers to the total amount of rainfall (mm); Q refers to total surface runoff (mm);
 159 S refers to the possible detention in the basin at that time (mm); CN refers to the number of
 160 runoff curves (dimensionless). The common dataset of the University of Maryland for global
 161 soil cover and the simplified International Geosphere–Biosphere Programme soil cover
 162 classification system were used to determine the runoff curve coefficient CN . Further, the
 163 hydrological soil groups of A, B, C, and D were determined according to the SCS soil
 164 classification.

165 The duration of runoff generation and the confluence and peak discharge were calculated by
 166 the rational formula of the Chinese Academy of Water Sciences (Eqs. (3)–(8)):

$$167 \quad \tau_0 = \left[\frac{0.278^{3/4}}{\frac{mJ^{1/3}}{L} (RF)^{1/4}} \right]^{4/4-n} = \left[\frac{0.383}{\frac{m}{\theta} R^{1/4}} \right]^{4/4-n} \quad (3)$$

$$168 \quad \psi = 1 - \frac{\mu}{R} \tau^n \quad (4)$$

$$169 \quad \mu = 3.6F^{-0.19} \quad (5)$$

170
$$\tau_c = \left[(1-n) \frac{R}{\mu} \right]^{\frac{1}{4-n}}$$
 (6)

171
$$\tau = \tau_0 \psi^{\frac{1}{4-n}}$$
 (7)

172
$$Q_p = 0.278 \psi i F = 0.278 \psi \frac{R}{\tau^n} F$$
 (8)

173 where ψ refers to the coefficient of flood-peak discharge (m^3/s); i refers to the maximum
 174 average rainstorm intensity (mm/h); R refers to the hourly rainfall (mm/h); n refers to the
 175 rainstorm index; F refers to the confluence area (km^2); L refers to the gully length (km); J
 176 refers to the gully-bed gradient; τ refers to the watershed confluence time (h); τ_0 refers to
 177 the watershed confluence time (h) when $\psi = 1$; τ_c refers to the runoff generation process at
 178 time (h), μ refers to the runoff generation parameter, i.e., the average infiltration intensity
 179 within the runoff generation process time (mm/h); m refers to the confluence parameter; Q_p
 180 refers to the peak discharge (m^3/s). According to the survey, the rainstorm index $n = 0.78$,
 181 the confluence area $F = 0.123 \text{ km}^2$, the gully length of the confluence area $L = 0.58 \text{ km}$,
 182 and the gully-bed gradient $J = 591\%$.

183 The rainstorm index was calculated by the rainstorm equation (Eqs. (9)–(11)) and was
 184 considered when the confluence lasted for 1 to 6 h.

185
$$H_{1p} = K_p \cdot \bar{H}_{1p}$$
 (9)

186 $H_{6p} = K_p \cdot \bar{H}_{6p}$ (10)

187 $n = 1 + 1.285 \lg\left(\frac{H_{1p}}{H_{6p}}\right)$ (11)

188 where, K_p is a rainfall coefficient, H_{np} refers to n hours of maximum rainfall (mm), \bar{H}
 189 refers to the average rainfall (mm).

190 **3.3 Numerical simulation of the CDH landslide at the origin of debris flow**

191 3D finite-difference software was used to calculate the dynamic response of the CDH under
 192 seepage flow at the source of the Chenghuangmiao Gully. Seepage and deformation were
 193 carried out simultaneously. The numerical model was established according to the field
 194 investigation of the CDH landslide (Table 1). The model consists of colluvium deposits, the
 195 bedrock, and the sliding surface, while comprising 7395 tetrahedral elements in total. The
 196 coupled deformation–diffusion processes was formulated within the quasi-static Biot theory
 197 framework, which can be applied to problems involving single-phase Darcy flow in a porous
 198 medium. Darcy’s law describes fluid transport (Eq.(12)) (Polubarinova-Kochina 1962):

199 $q_i = -k_{ij} \hat{k}(s) [p - \rho_f x_j g_j]_{,i}$ (12)

200 where q_i refers to the specific discharge vector, p refers to the pore pressure (Pa), k refers
 201 to the tensor of absolute mobility coefficients of the medium, $\hat{k}(s)$ refers to the relative

202 mobility coefficient, which is a function of fluid saturation, s , ρ_f refers to the fluid density
 203 (kg/m^3), and g_j , $i = 1, 3$ refers to the three components of the gravity vector.

204 The fluid mass balance is expressed as (Eq.(13)) (Biot 1956):

$$205 \quad -q_{i,j} + q_v = \frac{\partial \zeta}{\partial t} \quad (13)$$

206 where q_v refers to the volumetric fluid source intensity per second (m^3/s), and ζ refers to
 207 the variations in the fluid content or the fluid volume per unit volume of a porous material
 208 due to diffusive fluid transport as introduced by Biot (1956).

209 Changes in the variation of fluid content are related to changes in pore pressure, P ,
 210 saturation, s , and mechanical volumetric strains, ε . The response equation for the pore
 211 fluid is formulated as (Eq.(14)) (Keith et al. 1982):

$$212 \quad \frac{1}{M} \frac{\partial p}{\partial t} + \frac{n}{s} \frac{\partial s}{\partial t} = \frac{1}{s} \frac{\partial \zeta}{\partial t} - \alpha \frac{\partial \varepsilon}{\partial t} \quad (14)$$

213 where M refers to the Biot modulus (N/m^2), n refers to porosity, and α refers to the Biot
 214 coefficient.

215 After adding some modifications to the saturated fluid flow equation, we obtain the
 216 unsaturated fluid-flow equation in coarse soils (constant air pressure and no capillary
 217 pressure). The nodal volumetric flow rates in a zone Q_z are multiplied by relative mobility,

218 \hat{k} (see equation), which is a function ($\hat{k}(\hat{s}_{in}) = \hat{s}_{in}^2 (3 - 2\hat{s}_{in})$) of the average saturation at the

219 inflow nodes for the zone, \hat{s}_{in} . The gravity term $\rho_f x_i g_i$ is multiplied by the average zone
220 saturation to account for partial zone filling. Nodal inflow rates are scaled according to local
221 saturation. For unsaturated fluid flow, the nodal volumetric flow rates in a zone $\{Q_z\}$ are
222 related to the nodal pore pressures $\{p\}$, which is expressed in matrix notation as (Eq. (15)):
223 $\{Q_z \hat{k}\} = [M] \{p - \rho_f x_i g_i \bar{s}\}$ (15)
224 Because some updated physical and mechanical properties of soil are not considered in this
225 finite-difference software, and the sliding surface as a structural element is not affected by
226 pore pressure, the strength decreases (Ma et al. 2016; Schiliro et al. 2015). In this simulation,
227 the computer program is used to realise the change of sliding surface strength parameters
228 “ c ” and “ φ ” with saturation according to (Yang et al. 2014), which are updated every 100-
229 time steps. During the simulation, saturation, pore water pressure, and displacement of
230 different points in the CDH were monitored.

231 **Table 1**

232 Physical and mechanical parameters of rock and soil.

Type	Density (kg*m ⁻³)	Natural cohesion (kPa)	Natural friction angle (°)	Saturated cohesion (kPa)	Saturated friction angle (°)	Shear modulus (Pa)	Permeability coefficient(m/s)	Porosity
CDH	1980	33.4	23.6	6.7	8.5	1.5e6	3e-5	0.32
Bedrock	2201	2000	32			2.3e10	5e-10	0.24

233 3.4 Process of debris flow and calculation of motion feature parameters

234 The density of debris flow was calculated based on the clay content obtained from the soil
235 sieve analysis. We used the empirical formula of viscous debris-flow velocity to calculate
236 the flow velocity at different cross-sections based on cross-section investigation. We
237 obtained debris flow discharges at different cross-sections by combining the cross-section
238 features. According to the motion time of debris flow obtained from the survey, we used the
239 corrected pentagon method to calculate the total volume and solid volume of debris flow.
240 The density calculation method based on clay content is used to determine debris flow
241 density (Li et al. 2018) (Eq. (16)).

$$242 \gamma_c = -1.32 \times 10^3 x^7 - 5.13 \times 10^2 x^6 + 8.91 \times 10^2 x^5 - 55x^4 + 34.6x^3 - 67x^2 + 12.5x + 1.55 \quad (16)$$

243 where γ_c refers to the density of debris flow (g/cm^3); x refers to the percentage of clay
244 particles ($< 0.05 \text{ mm}$) in the total content of particles ($< 60 \text{ mm}$) in the debris flow deposits.
245 The flow velocity of debris flow was calculated by the cross-section investigation. During
246 the investigation, many drop weirs, bends, and bayonets were found, which were analysed as
247 high resistance viscous debris flow, and hence, the calculation formula is (Eq. (17)) [44].

$$248 V_c = (1/n_c) H_c^{2/3} I_c^{1/2} \quad (17)$$

249 where n_c refers to the roughness coefficient; H_c refers to the average mud depth (m); I_c refers
250 to the hydraulic gradient.

251 By combining the flow velocity with the cross-section area, we obtained the discharge (Eq.
252 (18)):

$$253 Q_c = A_{sc} * V_c \quad (18)$$

254 where A_{sc} refers to cross-section area (m^2); V_c refers to the velocity of debris flow of the
255 section (m/s).

256 We calculated the total volume of this continuous debris flow, and the modified Pentagon
257 method was used for the calculation [44]. According to the process time T and the maximum
258 flow Q_c of debris flow, the total volume of debris flow W_c is calculated by $W_c = KTQ_c$. The
259 solid volume of debris flow is calculated as follows (Eq. (19)):

$$260 W_s = C_v W_c = (\gamma_c - \gamma_w) W_c / (\gamma_s - \gamma_w) \quad (19)$$

261 where W_s refers to the solid volume of debris flow passed through the calculated section
262 (m^3); C_v refers to the volume concentration of the soil in the debris flow.

263 4 Features of debris flow in the Chenghuangmiao Gully

264 4.1 Features of debris-flow disaster

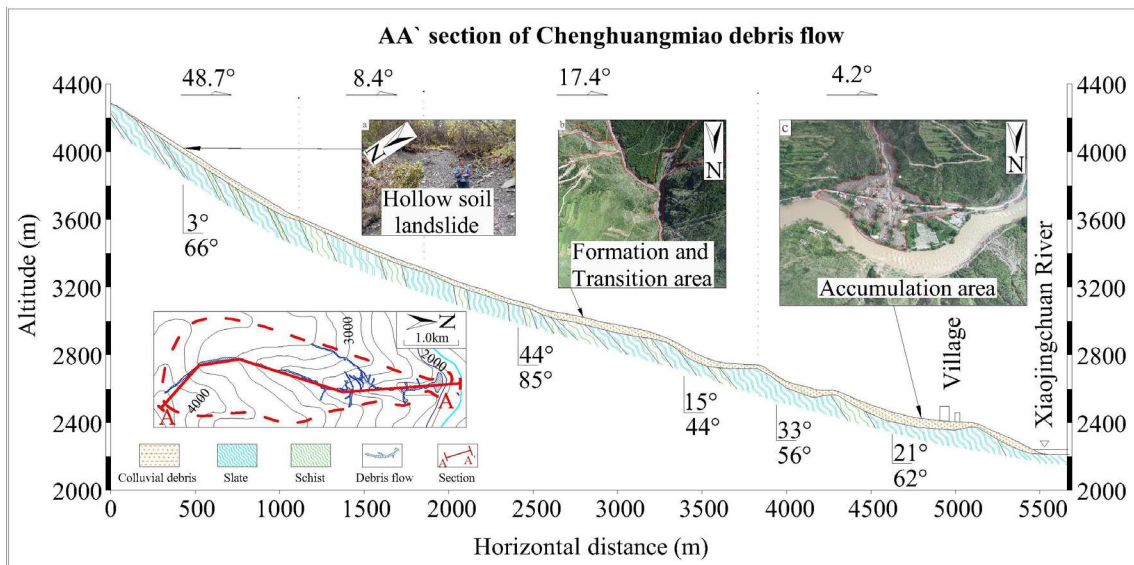
265 The Chenghuangmiao Gully debris-flow disaster was a giant low-frequency viscous
266 continuity delayed debris-flow disaster in a small watershed (Table 2).

267 Table 2

268 Parameters of debris flow in the Chenghuangmiao Gully.

Features	Watershed (m ³)	Peak discharge at mountain pass (m ³ /s)	Frequency (year/ once)	Density (g/cm ³)	Delay behind rainfall stop (h)	Death (person)
Value	6.10	290.4	1%	1.807	3.67	4
Property	Small	Giant	Low frequency	Viscosity	Delayed	Disaster

269 While the Chenghuangmiao Gully debris flow is recognised as a disaster, it is also a
270 geological process controlled by spatial distribution and temporal evolution features. The
271 horizontal and longitudinal sections of the Chenghuangmiao Gully show that it can be
272 divided into the CDH landslide at the gully source, initiation-circulation area, and
273 accumulation area (Fig. 4). After spatiotemporal considerations, we obtained the
274 accumulation and motion features of debris flow and the dynamic features of landslides at the
275 origin of the debris flow (the initiation process of debris flow).

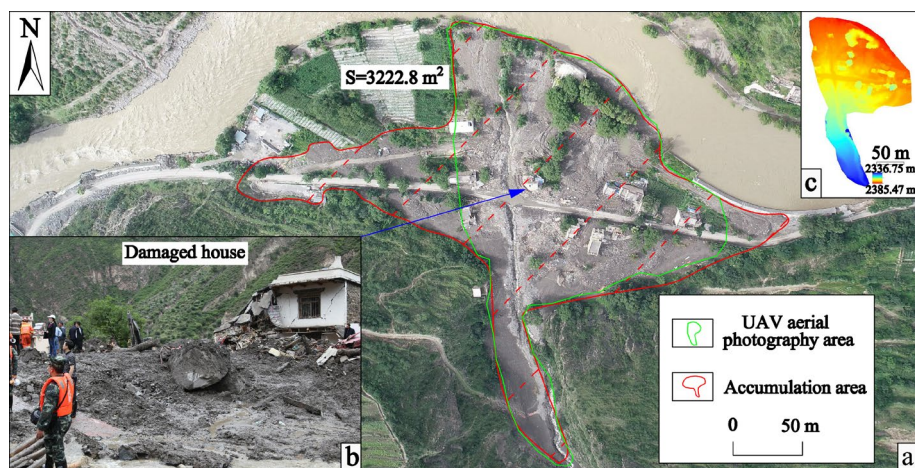


276
277 **Fig. 4.** Plan and longitudinal section of the Chenghuangmiao Gully: (a) CDH landslide at the
278 source of the Chenghuangmiao Gully; (b) Transition area; (c) Accumulation area.

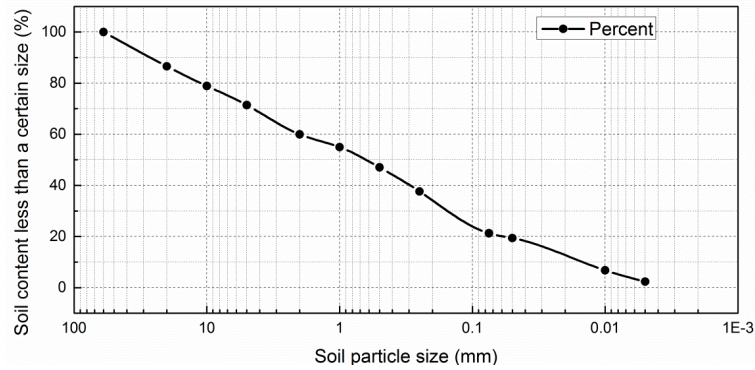
279 **4.2 Accumulation features of debris flow**

280 The debris flow experienced approximately 25 min of accumulation. After approximately
281 3200 m³ of debris-flow solid material was washed into the Xiaojinchuan river, the debris-
282 flow accumulation body of approximately 369.2 m in length, 198.3 m in width, 3222.8 m² in
283 area, 1.4–6.7 m in thickness, 159‰ in longitudinal gradient, and 18100 m³ of solid volume
284 (Fig. 5a–c) was formed. The deposits in the accumulation body were composed of slate and
285 schist fragments and clay. The deposits were well sorted, with 2.35% clay content and the
286 maximum boulder size was 3.0 × 2.7 × 1.8 m (Fig. 5b and Fig. 6).

287



288 **Fig. 5.** Accumulation area: (a) Accumulation area; (b) Washed-out houses; (c) Altitude
289 image.



290

291

Fig. 6. Debris flow accumulation particle curve.

292 4.3 Motion features and process of debris flow

293 The debris in the Chenghuangmiao Gully had a high density. There was an increase in the

294 initial velocity of debris flow and a later decrease, and a slow increase in its discharge. The

295 motion feature parameters were obtained through cross-section investigations, laboratory

296 tests, and theoretical model calculations. By incorporating 2.35% of clay content into the

297 empirical formula, we obtained a bulk density of 1.807 g/cm^3 for the debris flow. Based on

298 mud-mark height and gully-bed gradient obtained from the investigation of the debris-flow

299 gully, the viscous debris-flow velocity calculation formula (Eq. (16)) was used to obtain the

300 debris-flow peak velocity of 3.39–5.20 m/s (Table 3). Based on the cross-sectional area

301 obtained by the cross-sectional survey, the debris flow at different cross-sections was

302 calculated by (Eq. (17)). The peak debris flow was 57.6–290.4 m^3/s , with the maximum

303 occurring at the mountain pass (Fig. 7 and Table 3). Using the modified Pentagon method

304 (Eq. (18)) to calculate the total volume of debris flow, the total amount of debris flow W_c was

305 approximately 43995.6 m^3 , and the solid volume W_s was approximately 21260.2 m^3 .
 306 According to the investigation results, the total process time of debris flow was 25 min and
 307 the watershed area was 6.1 km^2 . The gully bed was rough and its average gradient was 375‰,
 308 and hence, $K = 0.0378$ and $1/n_c = 2.57$ in Eq. (17).

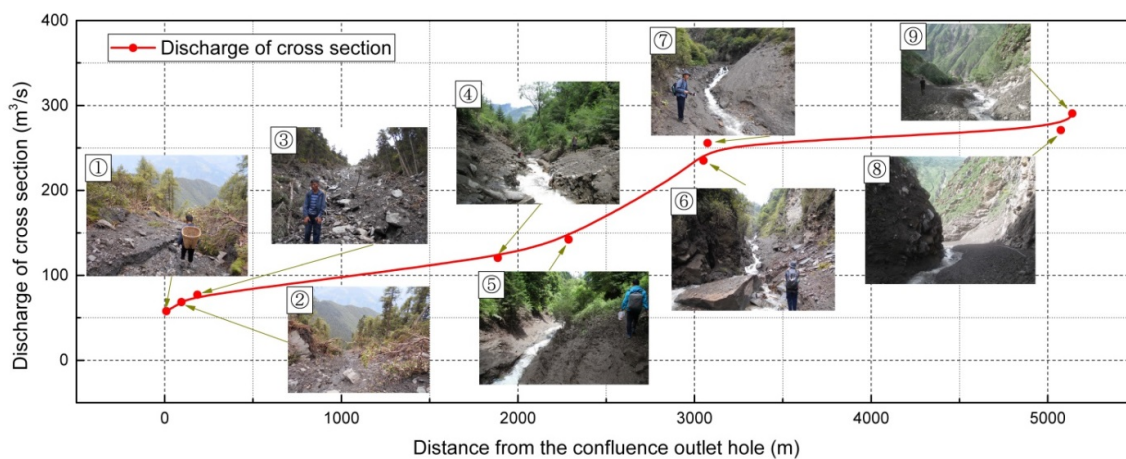
309 **Table 3**

310 The results of the calculation of flow by the morphological method.

Number	Section position	Hydraulic gradient	Maximum mud depth (m)	Area (m^2)	Velocity v_c ($\text{m}\cdot\text{s}^{-1}$)	Peak discharge ($\text{m}^3\cdot\text{s}^{-1}$)
1	102°10'38.16", 30°59'18.56"	0.68	2.1	17.0	3.39	57.6
2	102°10'36.11", 30°59'20.71"	0.68	2.3	18.5	3.69	68.3
3	102°10'31.71", 30°59'24.50"	0.82	2.5	18.0	4.06	77.2
4	102°10'16.14", 31°0'23.00"	0.34	4.6	29.1	4.15	120.5
5	102°10'21.36", 31°0'26.24"	0.29	5.2	34.2	4.15	141.9
6	102°10'31.16", 31°0'49.05"	0.21	7.2	53.5	4.39	234.9
7	102°10'31.67", 31°0'49.63"	0.55	4.5	49.2	5.20	255.6
8	102°10'32.73", 31°1'51.22"	0.27	6.2	58.0	4.68	270.9
9	102°10'32.35", 31°1'53.09"	0.36	4.3	66.2	4.39	290.4

311 The motion of debris flow in the main gully was a gradually increasing process of discharge,
 312 which took approximately 19.5 min. From section ① (about 0.01 km away from the CDH
 313 confluence outlet) (Fig. 8) to section ⑨ (at the mountain pass), the discharge slowly
 314 increased from $57.6 \text{ m}^3/\text{s}$ to $270.4 \text{ m}^3/\text{s}$. Combined with the average velocity of 4.23 m/s and
 315 the gully length of 4.95 km, the time of the debris flow was calculated at approximately 19.5
 316 min.

317 Between section ④ (about 2 km away from the outlet of the CDH confluence) and section
 318 ⑦ (about 3 km away from the outlet of the CDH confluence), the discharge process line
 319 became steeper (discharge increased from 141.9 m³/s to 234.9 m³/s). By combining the
 320 increase in the hydraulic gradient observed by the two sections (increased from
 321 approximately 340‰ to approximately 550‰), the expansion of the sectional area, and the
 322 rise in the thickness of the loose deposits, we found that the increase in discharge was due to
 323 an increase in the hydraulic gradient and material sources. The debris flow in the
 324 Chenghuangmiao Gully was not limited or blocked (Fig. 7).



325

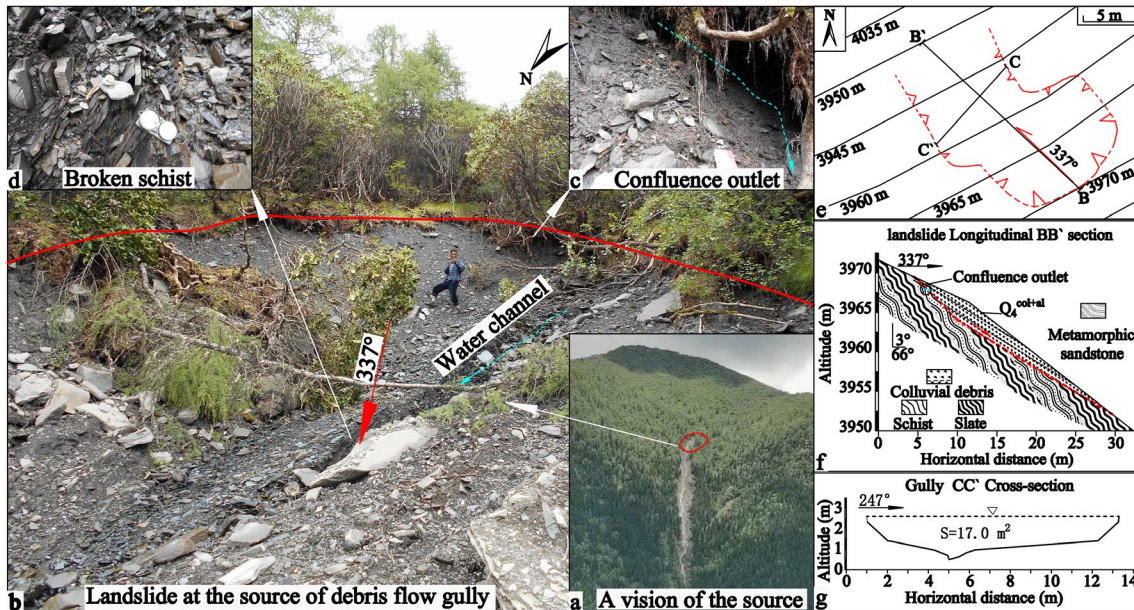
326

Fig. 7. Debris flow discharge process.

327 4.4 Features of the CDH landslide at the origin of debris flow

328 The CDH landslide at the origin of debris flow was a small shallow soil landslide. The
 329 landslide was located at the outlet of the CDH confluence area (102°10'38.16" and
 330 30°59'18.56") at an altitude of 4060 m (Fig. 8a). The slide body was composed of crushed

331 rock and soil. The length, width, thickness, area, and volume of the slide body were 25.0 m,
332 12.3 m, 1.1–1.8 m, 296 m², and 362 m³, respectively. The angle between the sliding direction
333 (337°) and bedrock inclination (3°) was 26°. The sliding surface was the interface of bedrock
334 and deposits. The trailing edge was 7.7 m long and the slope was 45° (Fig. 8b–h). The
335 bedrock occurred on the slide bed at an angle of 3° < 66°. Slate and schist alternately
336 appeared, the slate was bent, sericite was seen on the layer, scratches were developed, schist
337 joints were broken, and the water flowed along with the schist layer towards the toe of the
338 CDH (Fig. 8b–d). The hole at the CDH confluence outlet was located at the junction of the
339 rear edge and the left boundary. The soil on the upper part of the outlet had not sunk owing to
340 the development of moss, the outlet hole was 2.4 m wide, the highest was at 0.8 m, and the
341 lowest was at 0.5 m and the cross-sectional area was 1.56 m² (Fig. 8c). With the downward
342 sliding of the landslide, a bedrock block appeared on the landslide's right boundary, which
343 decreased by 4.8 m horizontally, and the left boundary of the landslide widened by 2.1 m
344 southwest (Fig. 8e).



345 **Fig. 8.** The CDH landslide at the source of the debris-flow gully; (a) The location of the CDH
 346 landslide at the source of the gully; (b) The trailing edge of the CDH landslide at the source
 347 of the gully and the slide bed; (c) The bedrock on the slide bed; (d) The confluence outlet; (e)
 348 Landslide plan; (f) Landslide profile; (g) Landslide cross-section.

350 5 Initiation of delayed debris flow

351 The initiation of debris flow was delayed by the landslide process of the CDH at the back-end
 352 confluence. Rainfall mainly converged on to the CDH in the form of surface and subsurface
 353 runoff. Under the effect of water infiltration, the saturation and pore pressure of the CDH
 354 increased, the intensity decreased, and instability occurred resulting in the landslide, and that
 355 initiated the debris flow. The whole process took 9 h 20 min from 18:00 h on 5 July 2020 to
 356 03:20 h on 6 July 2020.

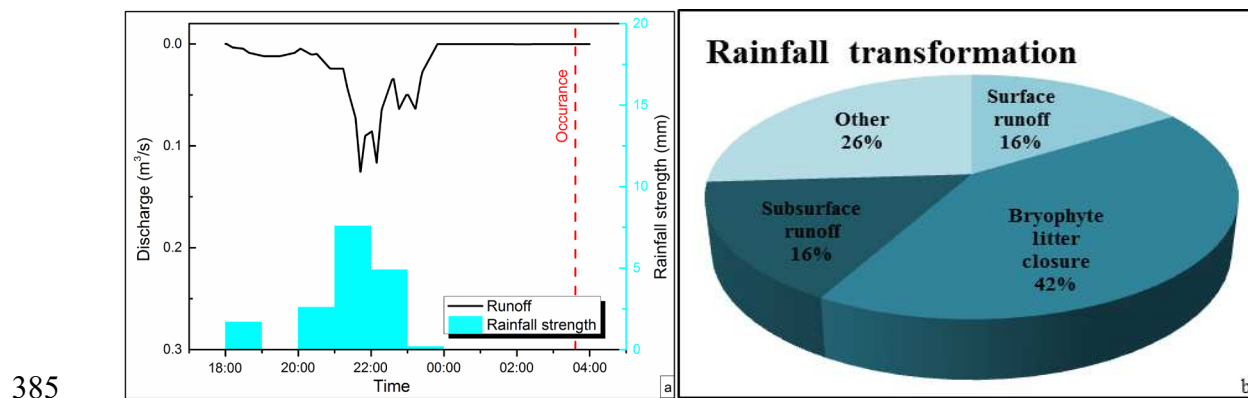
357 The reasons for the occurrence of debris flow in the Chenghuangmiao Gully 3 h 40 min after
358 the rainfall stopped is as follows: Rainfall and confluence infiltrations during the rainfall
359 could not sufficiently increase the pore pressure of the CDH and weaken it to cause
360 instability. The seepage process continued for 3 h 20 min inside the CDH after the rainfall
361 stopped. That was sufficient to increase the pore pressure of the CDH and reduce its strength
362 causing instability, thereby initiating the debris flow.

363 **5.1 Surface runoff and subsurface flow process at the back end of the CDH**

364 The back-end confluence was the rainfall entering the CDH in the form of surface and
365 subsurface runoff. The effective rainfall amount that was transformed into surface and
366 subsurface runoff before the disaster was 32%. The confluence lasted approximately 5.76 h,
367 and the peak flow was 0.125 m³/s at 21:42 on 5 July 2020, and the rest of the rainfall was
368 intercepted and evaporated by moss litter and others.

369 The above data were obtained by the following calculation or empirical method: 1) Using the
370 SCS model to calculate the effective rainfall (17 mm) from 18:00 to 24:00 h on 5 July 2020
371 produced a total surface runoff of 2.729 mm, that is, surface runoff accounted for 16.05% of
372 the total rainfall (Eqs. (1) and (2)); 2) Based on the rational formula (Eqs. (3)–(11)), the five-
373 hours peak flow and runoff time were obtained (Table 4); 3) By combining 16.05% runoff
374 yield ratio, peak flow, and runoff time, the pentagon process line was used to generalise the
375 surface-runoff process per hour, and then, the surface runoff flow process line was obtained;

376 4) According to results of the experimental research on surface and subsurface runoff
 377 conducted by Li et al., the process of subsurface runoff was similar to the process of surface
 378 runoff, and the delay was 26.5 min in the study area (Li et al. 2010; Zhang et al. 2015), and
 379 then, we obtained the subsurface-runoff process line according to the surface-runoff process
 380 line; 5) By superimposing the surface-runoff process line and the subsurface-runoff process
 381 line, the runoff process of the confluence at the back end of the CDH was obtained (Fig. 9a);
 382 6) Based on the research of Ye et al., the interception of the moss litter layer with a thickness
 383 of 9.8 cm in the study area accounted for approximately 42% of the total rainfall (Wang et al.
 384 2010; Ye et al. 2004). Finally, the pie chart of the rainfall distribution was prepared (Fig. 9b).



386 **Fig. 9.** Rainfall and runoff: (a) Runoff process line at the back end of the CDH; (b) Rainfall
 387 transformation pie chart.

388 **Table 4**

389 Results of the calculations of confluence parameters using the rational formula.

Time	Peak discharge Q_p ($m^3 \cdot s^{-1}$)	Surface runoff (m^3)	Runoff generation time τ_c (h)	Confluence time τ (h)
19:00	0.0069	33.56	0.035	2.029
20:00	0.0000	0.00	0.000	0.000
21:00	0.0157	51.33	0.064	1.651
22:00	0.1141	150.04	0.236	0.935
23:00	0.0538	96.73	0.162	1.210
24:00	0.0001	0.98	0.002	5.864

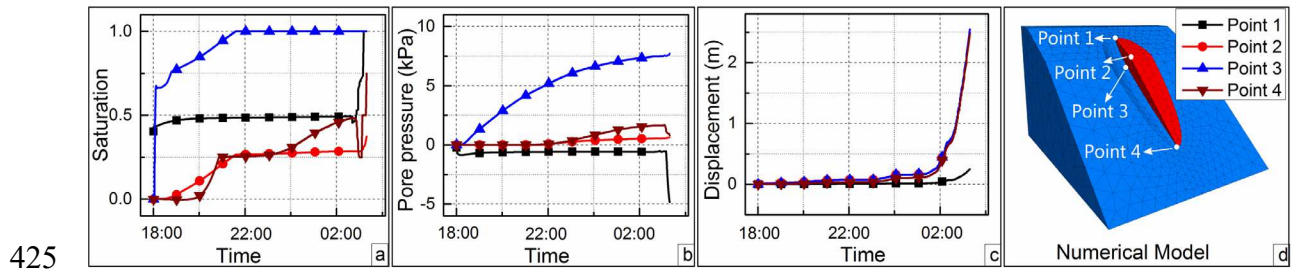
390 5.2 Initiation of debris flow induced by CDH landslide

391 The initiation of debris flow was caused by an increase in the pore water pressure of the CDH
392 and decrease in its strength after the confluence and rainfall infiltration, and the CDH
393 landslide entered the accelerated deformation stage. The rainfall from 18:00 to 24:00 h on 5
394 July 2020 caused surface and subsurface runoff to continuously converge into the CDH; on
395 saturation, the CDH expanded rapidly along with the base interface to the leading edge,
396 causing the pore pressure of the soil near the base interface to increase. The rain stopped from
397 00:00 to 03:20 h on 6 July 2020, and the expansion of the saturation range of the CDH
398 became slower, and eventually it made the soil near the leading edge and base interface
399 saturated, thereby decreasing the soil strength, causing the CDH landslide, and subsequently
400 initiating the debris flow.

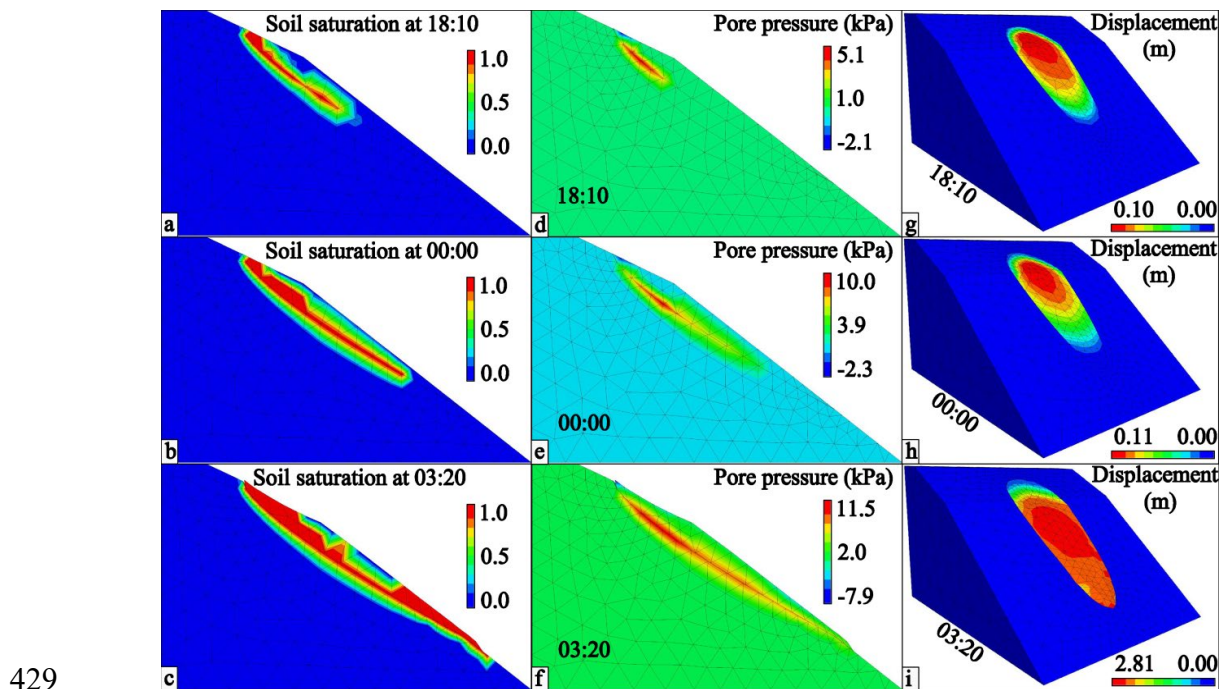
401 The changes in soil saturation, pore water pressure, and displacement reflected the changes in
402 the soil's state. Saturation at Point 1 in the trailing edge of CDH, Point 2 in the near-surface
403 of the middle part of CDH, and Point 3 in the near base interface of the middle part of CDH
404 increased first, and then, remained stable. Point 3 reached saturation first. Saturation at Point

405 4 was rising throughout the process, and the range of saturation expanded, and at
406 approximately 03:20 h the saturation at each point increased sharply (Fig. 10a, Fig. 11a–c).
407 The changes in pore pressure and saturation were similar. Pore pressure at Point 3 increased
408 the fastest, from 0.0 kPa to 7.2 kPa, while the pore pressure at the other points increased
409 slowly and decreased sharply at approximately 03:20 h. During the whole process, the value
410 of pore pressure increased and the range of positive pore pressure increased (Fig. 10b, Fig.
411 11e–g). These changes in saturation and pore pressure caused the near base interface part of
412 the CDH to become the main seepage channel. The seepage channel caused the continuous
413 infiltration in the leading edge of the CDH. The strength at the leading edge and the soil near
414 the base interface of the CDH reduced resulting in the landslide. The displacement of the
415 monitoring points shows the process of landslide instability and deformation that initiated the
416 debris flow. The displacement of each point of the CDH showed an increasing trend during
417 and after the rain stopped and increased by 0.03, 0.25, 0.26, 0.26 m respectively at the four
418 points at 02:00 h on 6 July 2020. After 02:00 h on 6 July 2020 the displacement at each point
419 increased sharply. The rate of displacement at each point from 02:18 to 02:50 h decreased
420 slightly, and the displacement curve showed a stable and rapid increase from 02:50 to 03:20 h
421 (Fig. 10c, Fig. 11g–i). According to (Azimi et al. 1988; Tavenas and Leroueil 1981), we
422 divided the stages of slope deformation and failure. We found that the initial deformation

423 stage occurred from 02:00 to 02:18 h, the secondary deformation stage occurred from 02:18
 424 to 02:50 h, and the accelerated deformation stage occurred from 02:50 to 03:20 h.



426 **Fig. 10.** Variation of the CDH parameters at different locations with time: (a) Soil saturation
 427 variation curve; (b) Pore water pressure variation curve; (c) Deformation displacement
 428 variation curve; (d) Numerical model.



430 **Fig. 11.** The CDH landslide simulation results: (a) Soil saturation at 18:10 h; (b) Soil
431 saturation at 00:00 h; (c) Soil saturation at 03:20 h; (d) Pore water pressure distribution at
432 18:10 h; (e) Pore pressure distribution at 00:00 h; (f) Pore pressure distribution at 03:20 h; (g)
433 Total soil deformation at 18:10 h; (h) Total soil deformation at 00:00 h; (i) Total soil
434 deformation at 03:20 h.

435 The debris flow reached the gully mouth at 03:40 h by field investigation, and the debris
436 flow took 19.5 min by calculation; hence, the debris flow was initiated at about 03:20 h.
437 Therefore, the accuracy of the simulation was verified.

438 **6 Conclusions and Discussions**

439 Since 18:00 h on 5 July 2020, rainfall mainly converged into the CDH in the form of surface
440 and subsurface runoff, and the pore pressure of the CDH increased and its strength decreased.
441 At 02:00 h on 6 July 2020, the CDH showed obvious deformation signs and entered the
442 initial deformation stage of the landslide. At 03:20 h on 6 July 2020, the displacement of each
443 point of the CDH increased sharply, the CDH landslide entered the accelerated deformation
444 stage, and the debris flow was initiated. At 03:40 h on 6 July 2020, viscous debris flow
445 experienced a gradual increase in its discharge motion for approximately 19.5 min, reaching
446 Yuanying Village, Xiaojin County. At 04:05 on 6 July 2020, the debris flow that lasted for 25
447 min ended, causing 4 deaths and 27 injuries.

448 We studied the delayed debris flow that occurred recently in the Chenghuangmiao Gully at
449 Aba Prefecture of Sichuan Province. Through field investigations, laboratory tests, theoretical
450 calculations, and fluid–solid coupling numerical simulation based on Biot theory, the motion
451 features and the initiation of the debris flow were analysed based on surface and subsurface
452 runoff (at the back end), and the instability and landslide process of the CDH. Therefore, the
453 following conclusions were reached.

454 (1) The Chenghuangmiao Gully debris-flow disaster was a giant viscous continuous
455 delayed low-frequency debris-flow disaster in a small watershed. The density of the debris
456 flow was 1.807 g/cm^3 , which occurs only once in a century by investigation. The maximum
457 velocity of the debris flow was 5.2 m/s , max discharge at the mountain pass was $290.4 \text{ m}^3/\text{s}$,
458 and debris flow volume was approximately $44,000 \text{ m}^3$.

459 (2) The CDH landslide at the source of the Chenghuangmiao Gully was a small shallow
460 soil landslide. The sliding direction of the landslide was 337° , and its sliding surface was the
461 base interface; it exhibited an area of 296 m^2 , with the sliding volume being 362 m^3 .

462 (3) The initiation of debris flow was represented by the delayed landslide process of the
463 CDH under the influence of back-end confluence. Rainfall flowed into the CDH in the form
464 of surface and subsurface runoff. The pore pressure of the CDH rose, and its strength
465 decreased. The CDH landslide entered the accelerated deformation stage to initiate debris
466 flow. The whole process took 9 h and 20 min.

467 (4) The motion of debris flow in the main gully represented a process that slowly
468 increased discharge, which took approximately 19.5 min.

469 (5) Rainfall and confluence infiltration were insufficient to reduce the pore pressure and
470 increase instability of the CDH, thereby causing the delay in debris flow. After the rainfall
471 stopped, the seepage process continued for 3 h 20 min inside the soil, and it increased the
472 pore pressure of the soil sufficiently and reduced the strength of the CDH to initiate the debris
473 flow.

474 The evacuation of personnel from vulnerable areas should form the core of the process of
475 prevention and mitigation of a debris-flow disaster event. There is a need to perform
476 comprehensive disaster investigation, provide measures for active prevention, identify and
477 control hidden danger points, achieve passive relocation, and execute continuous monitoring
478 of debris flow confluence area (Shimizu area), which can effectively reduce the losses caused
479 by delayed debris flow. The investigation of debris-flow gully in the confluence area
480 (Shimizu area) is required. After identifying the hidden dangers of geological disasters and
481 assessing the disaster risks, timely, preventive, and passive avoidance measures must be
482 undertaken. When rainfall occurs at the hidden point and disappears for a few hours, it is
483 necessary to continuously monitor the debris-flow source area and confluence area (Shimizu
484 area) afterward, and issue early warnings in time. Finally, strengthening of the management

485 and control of evacuation measures is necessitated to ensure the cessation of human activity
486 within the danger zone before the disaster occurs.

487 **Acknowledgements**

488 This work was supported by the National Key Research and Development Program of China
489 [grant number 2018YFC1505202]; the National Natural Science Foundation of China [gran
490 t number U20A20110]; and the Youth Innovation Promotion Association CAS [grant numb
491 er 2020367].

492 **Declaration of interests**

493 The authors declare that they have no known competing financial interests or personal relati
494 onships that could have appeared to influence the work reported in this paper.

495 **References**

- 496 Alfieri L, Laio F, Claps P (2008) A simulation experiment for optimal design hyetograph selection Hydrological
497 Processes 22:813-820 doi:10.1002/hyp.6646
- 498 Azimi C, Biarez J, Desvarreux P, Keime F Prevision d'eboulement en terrain gypseux. In: International
499 symposium on landslides. 5, 1988. pp 531-536
- 500 Baum RL, Godt JW (2010) Early warning of rainfall-induced shallow landslides and debris flows in the USA
501 Landslides 7:259-272 doi:10.1007/s10346-009-0177-0
- 502 Biot MA (1956) General solutions of equations of elasticity and consolidation for a porous material Journal of
503 Applied Mechanics 23:91-96
- 504 Cannon SH, Boldt EM, Laber JL, Kean JW, Staley DM (2011) Rainfall intensity-duration thresholds for postfire
505 debris-flow emergency-response planning Natural Hazards 59:209-236 doi:10.1007/s11069-011-9747-
506 2
- 507 Cannon SH, Gartner JE, Wilson RC, Bowers JC, Laber JL (2008) Storm rainfall conditions for floods and debris
508 flows from recently burned areas in southwestern Colorado and southern California Geomorphology
509 96:250-269 doi:10.1016/j.geomorph.2007.03.019
- 510 Chen N, Zou Q, Su F, Cui P, Zhang Y (2015) Risk assessment and disaster reduction strategies for mountainous
511 and meteorological hazards in Tibetan Plateau Chinese Science Bulletin 60:3067-3077
512 doi:10.1360/n972015-00849
- 513 Chen NS, Yue ZQ, Cui P, Li ZL (2007) A rational method for estimating maximum discharge of a landslide-
514 induced debris flow: A case study from southwestern China Geomorphology 84:44-58
515 doi:<https://doi.org/10.1016/j.geomorph.2006.07.007>
- 516 Clark CO (1945) STORAGE AND THE UNIT HYDROGRAPH Transactions of the American Society of Civil
517 Engineers 110:1419-1446

518 Crosta GB, Dal Negro P (2003) Observations and modelling of soil slip-debris flow initiation processes in
519 pyroclastic deposits: the Sarno 1998 event *Natural Hazards and Earth System Sciences* 3:53-69
520 doi:10.5194/nhess-3-53-2003

521 Deng QL, Zhu ZY, Cui ZQ, Wang XP (2000) Mass rock creep and landsliding on the Huangtupo slope in the
522 reservoir area of the Three Gorges Project, Yangtze River, China *Engineering Geology* 58:67-83
523 doi:10.1016/s0013-7952(00)00053-3

524 Edward Kuiper C.I. SM, P.Eng., F.ASCE, MEIC (1965) *Water Resources Development*. Springer US,

525 Feng Z, Cui P, He S (2005) Mechanism of conversion of landslides to debris flows *Journal of Natural Disasters*
526 14:8-14

527 Guzzetti F, Peruccacci S, Rossi M, Stark CP (2008) The rainfall intensity-duration control of shallow landslides
528 and debris flows: an update *Landslides* 5:3-17 doi:10.1007/s10346-007-0112-1

529 Hua JP, Liang ZM, Yu ZB (2003) A modified rational formula for flood design in small basins *Journal of the*
530 *American Water Resources Association* 39:1017-1025 doi:10.1111/j.1752-1688.2003.tb03689.x

531 Huang R, Pei X, Fan X, Zhang W, Li S, Li B (2012) The characteristics and failure mechanism of the largest
532 landslide triggered by the Wenchuan earthquake, May 12, 2008, China *Landslides* 9:131-142
533 doi:10.1007/s10346-011-0276-6

534 Iverson RM (1997) The physics of debris flows *Reviews of Geophysics* 35:245-296 doi:10.1029/97rg00426

535 Iverson RM, Denlinger RP (2001) Flow of variably fluidized granular masses across three-dimensional terrain
536 1. Coulomb mixture theory *Journal of Geophysical Research-Solid Earth* 106:537-552
537 doi:10.1029/2000jb900329

538 Iverson RM, Reid ME, LaHusen RG (1997) Debris-flow mobilization from landslides *Annual Review of Earth*
539 *and Planetary Sciences* 25:85-138 doi:10.1146/annurev.earth.25.1.85

540 Iverson RM, Vallance JW (2001) New views of granular mass flows *Geology* 29:115-118 doi:10.1130/0091-
541 7613(2001)029<0115:nvogmf>2.0.co;2

542 Keith, Beven, Peter, Germann (1982) Macropores and water flow in soils *Water Resources Research*

543 Kim MS, Onda Y, Uchida T, Kim JK, Song YS (2018) Effect of seepage on shallow landslides in consideration
544 of changes in topography: Case study including an experimental sandy slope with artificial rainfall
545 *Catena* 161:50-62 doi:10.1016/j.catena.2017.10.004

546 Lee ML, Ng KY, Huang YF, Li WC (2014) Rainfall-induced landslides in Hulu Kelang area, Malaysia *Natural*
547 *Hazards* 70:353-375 doi:10.1007/s11069-013-0814-8

548 Li C, Zhu J, Wang B, Jiang Y, Liu X, Zeng P (2016) Critical deformation velocity of landslides in different
549 deformation phases *Chinese Journal of Rock Mechanics and Engineering* 35:1407-1414

550 Li J, Cai Q, Sun L, Chen X (2010) Reviewing on Factors and Critical Conditions of Rill Erosion *Progress in*
551 *Geography* 29:1319-1325

552 Li J, Chen N, Iqbal J, Han D (2018) Model for Dilution Process of Landslide Triggered Debris Flows -A Case in
553 the Guanba River, Southeastern Tibetan Plateau *Earth Sciences Research Journal* 22:103-111
554 doi:10.15446/esrj.v22n2.68177

555 Ma D et al. (2016) Effect of mining on shear sidewall groundwater inrush hazard caused by seepage instability
556 of the penetrated karst collapse pillar *Natural Hazards* 82:73-93 doi:10.1007/s11069-016-2180-9

557 Mishra SK, Singh VP (2003) SCS-CN Method. In: *Soil conservation service curve number (SCS-CN)*
558 *methodology*. Springer, pp 84-146

559 Pegram G, Parak M (2004) A review of the regional maximum flood and rational formula using
560 geomorphological information and observed floods *Water Sa* 30:377-392

561 Polubarinova-Kochina P (1962) *Theory of Groundwater Movement* (trans: de Wiest, JMR) Princeton University
562 Press. Princeton,

563 Qi S, Yan F, Wang S, Xu R (2006) Characteristics, mechanism and development tendency of deformation of
564 Maoping landslide after commission of Geheyan reservoir on the Qingjiang River, Hubei Province,
565 China Engineering Geology 86:37-51 doi:10.1016/j.enggeo.2006.04.004

566 Qiang XU, Minggao T, Kaixiang XU, Xuebin H (2008) RESEARCH ON SPACE-TIME EVOLUTION LAWS
567 AND EARLY WARNING-PREDICTION OF LANDSLIDES Chinese Journal of Rock Mechanics and
568 Engineering 27:1104-1112

569 Schiliro L, Esposito C, Mugnozsa GS (2015) Evaluation of shallow landslide-triggering scenarios through a
570 physically based approach: an example of application in the southern Messina area (northeastern Sicily,
571 Italy) Natural Hazards and Earth System Sciences 15:2091-2109 doi:10.5194/nhess-15-2091-2015

572 Singh TN, Gulati A, Dontha L, Bhardwaj V (2008) Evaluating cut slope failure by numerical analysis - a case
573 study Natural Hazards 47:263-279 doi:10.1007/s11069-008-9219-5

574 Tavenas F, Leroueil S (1981) Creep and failure of slopes in clays Canadian Geotechnical Journal 18:106-120
575 doi:10.1139/t81-010

576 Wang X, Ye J, Li B, Zhang J, Lin F, Hao Z (2010) Spatial distributions of species in an old-growth temperate
577 forest, northeastern China Canadian Journal of Forest Research 40:1011-1019 doi:10.1139/x10-056

578 Yang H, Wang X, Xiao J (2014) Influence of wetting-drying cycles on strength characteristics of Nanning
579 expansive soils Chinese Journal of Geotechnical Engineering 36:949-954

580 Ye J, Hao Z, Jiang P (2004) Studies on rainfall holding process of the bryophyte and litter layer in coniferous
581 forest of Changbai Mountain Acta Ecologica Sinica 24:2859-2862

582 Yue H, Liu F, Yan Z (2012) Approaches to Estimate Peak-discharges by Rainfall in Small to Medium Scale
583 River Basins Journal of Sichuan University Engineering Science Edition 44:39-44

584 Zhang Y, Chen N, Liu M, Wang T, Deng M, Wu K, Khanal BR (2019) Debris flows originating from colluvium
585 deposits in hollow regions during a heavy storm process in Taining, southeastern China Landslides
586 17:335-347 doi:10.1007/s10346-019-01272-x

587 Zhang Z, Sheng L, Yang J, Chen X-A, Kong L, Wagan B (2015) Effects of Land Use and Slope Gradient on
588 Soil Erosion in a Red Soil Hilly Watershed of Southern China Sustainability 7:14309-14325
589 doi:10.3390/su71014309

590 Zhou D, Zhang Z, Li J, Wang X (2019) Seepage-stress coupled modeling for rainfall induced loess landslide
591 Theoretical and Applied Mechanics Letters 9:7-13 doi:10.1016/j.taml.2019.02.006

592

Figures

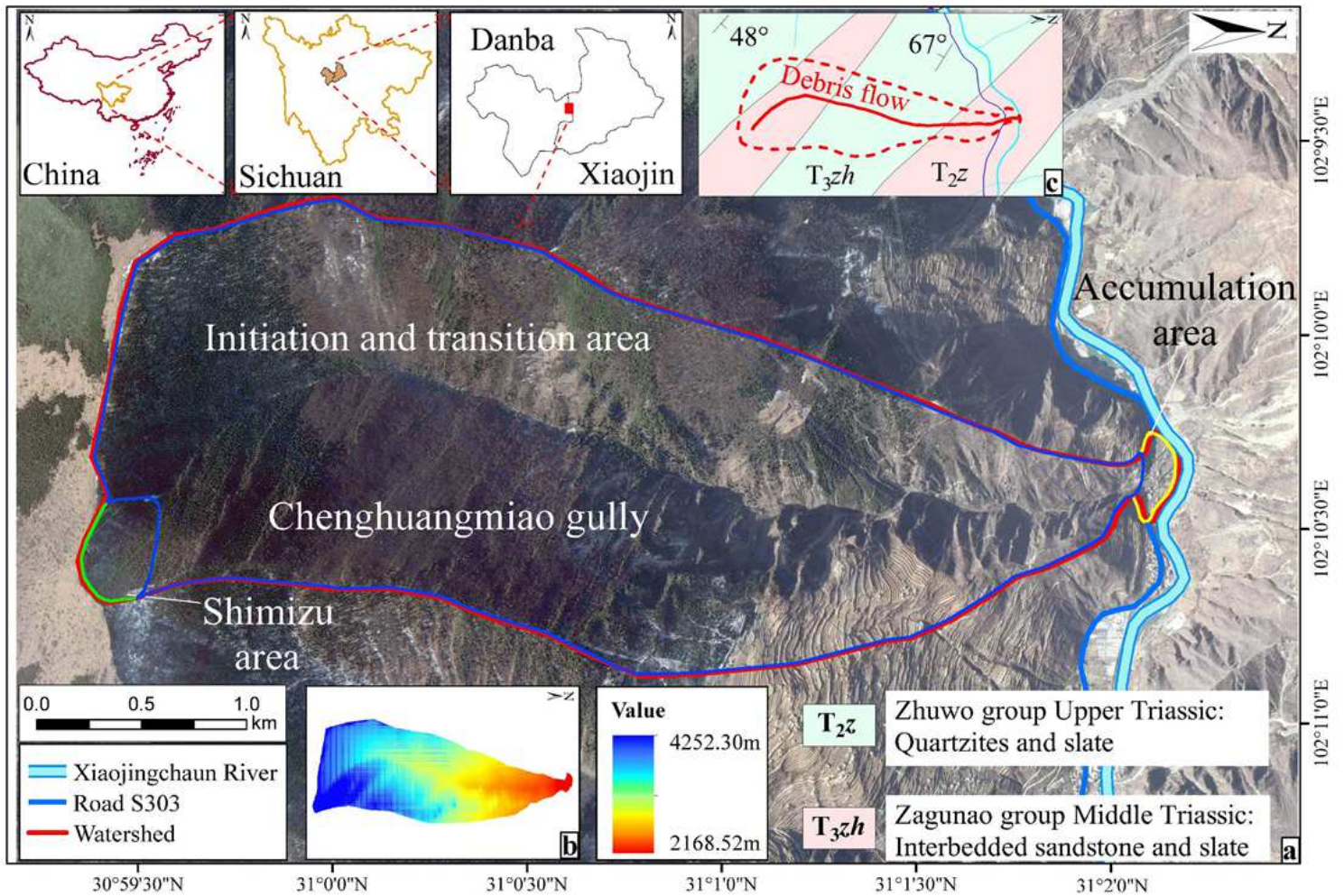


Figure 1

Chenghuangmiao Gully: (a) watershed; (b) altitude; (c) geological map. Note: The designations employed and the presentation of the material on this map do not imply the expression of any opinion whatsoever on the part of Research Square concerning the legal status of any country, territory, city or area or of its authorities, or concerning the delimitation of its frontiers or boundaries. This map has been provided by the authors.

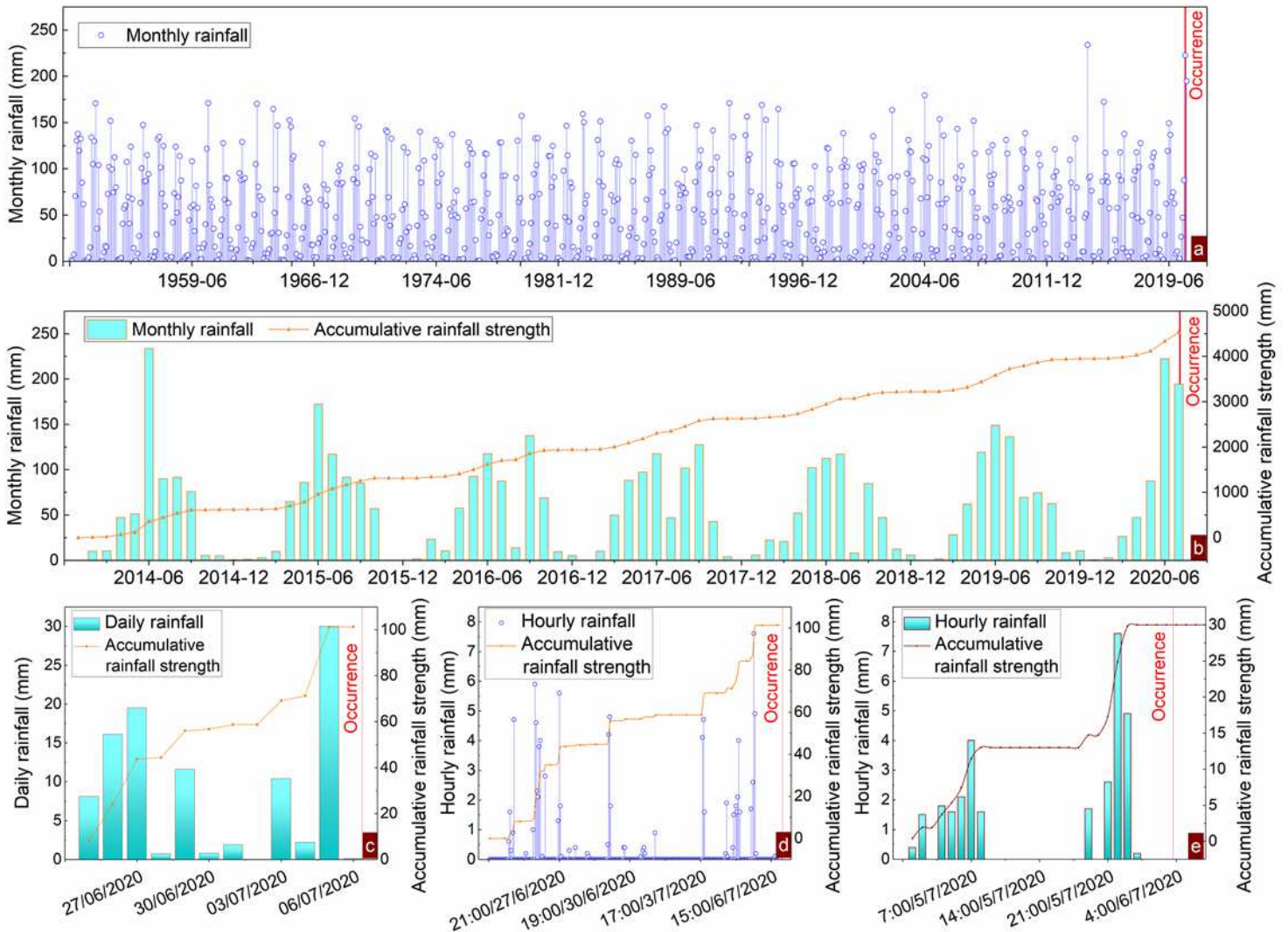


Figure 2

Rainfall trends in the study area: (a) Monthly rainfall from 1952; (b) Monthly rainfall from 2014 to 2020; (c) Daily rainfall in the 12 days before the occurrence of debris flow; (d) Hourly rainfall in the 12 days before the occurrence; (e) Hourly rainfall 30 h before the occurrence.

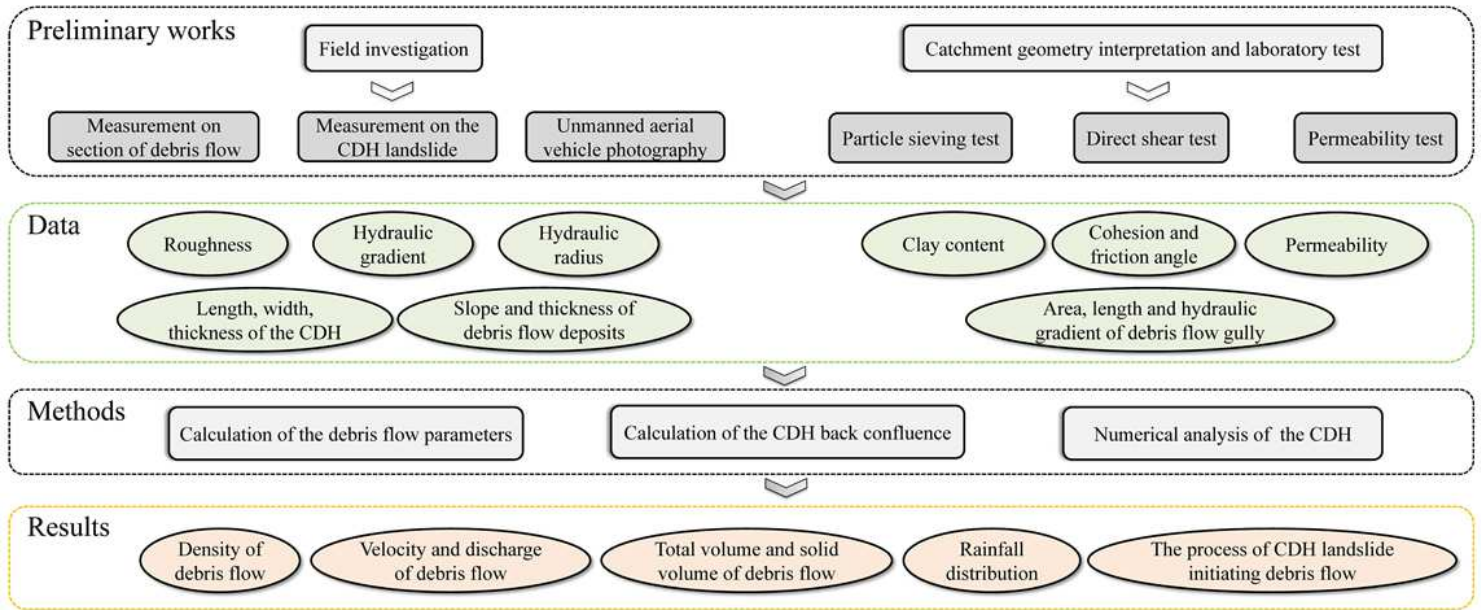


Figure 3

Methodology used to analyse the initiation of debris flow.

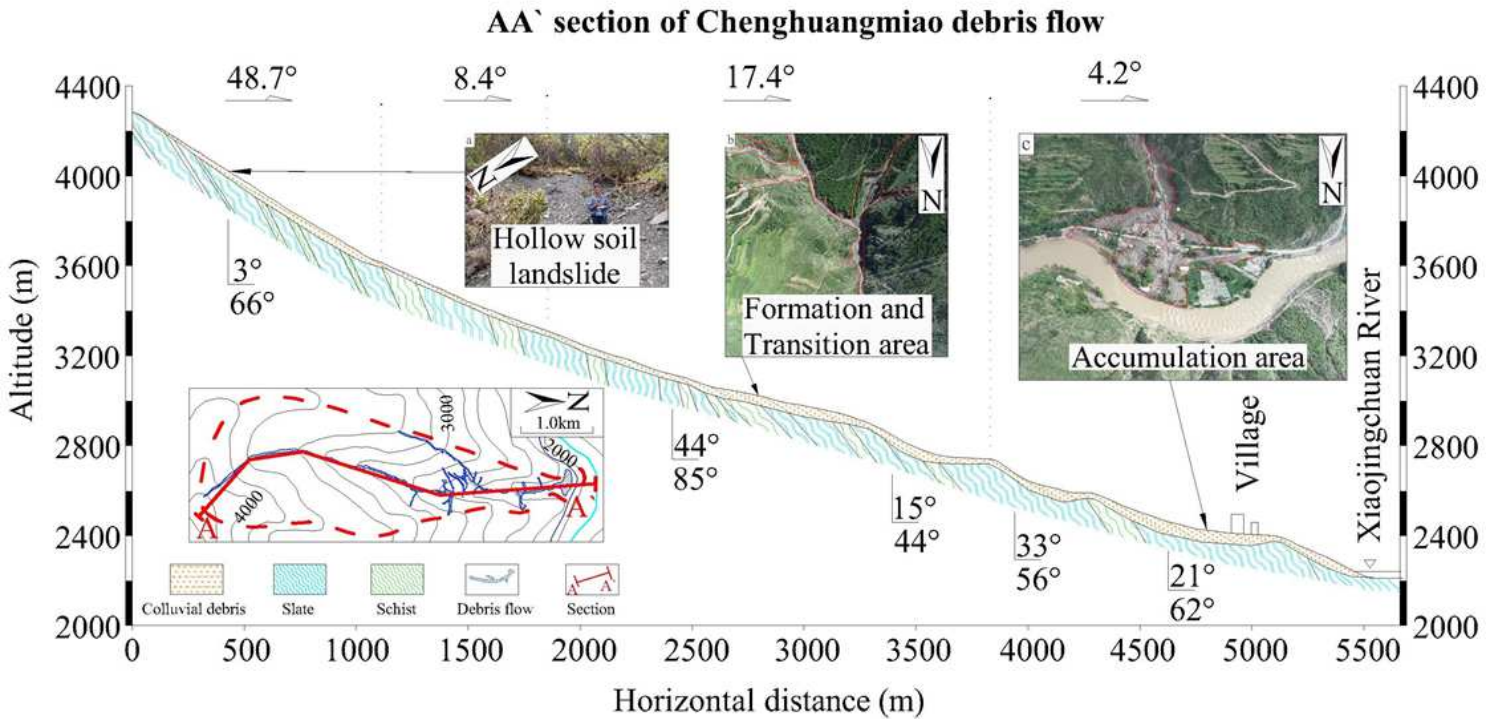


Figure 4

Plan and longitudinal section of the Chenghuangmiao Gully: (a) CDH landslide at the source of the Chenghuangmiao Gully; (b) Transition area; (c) Accumulation area.

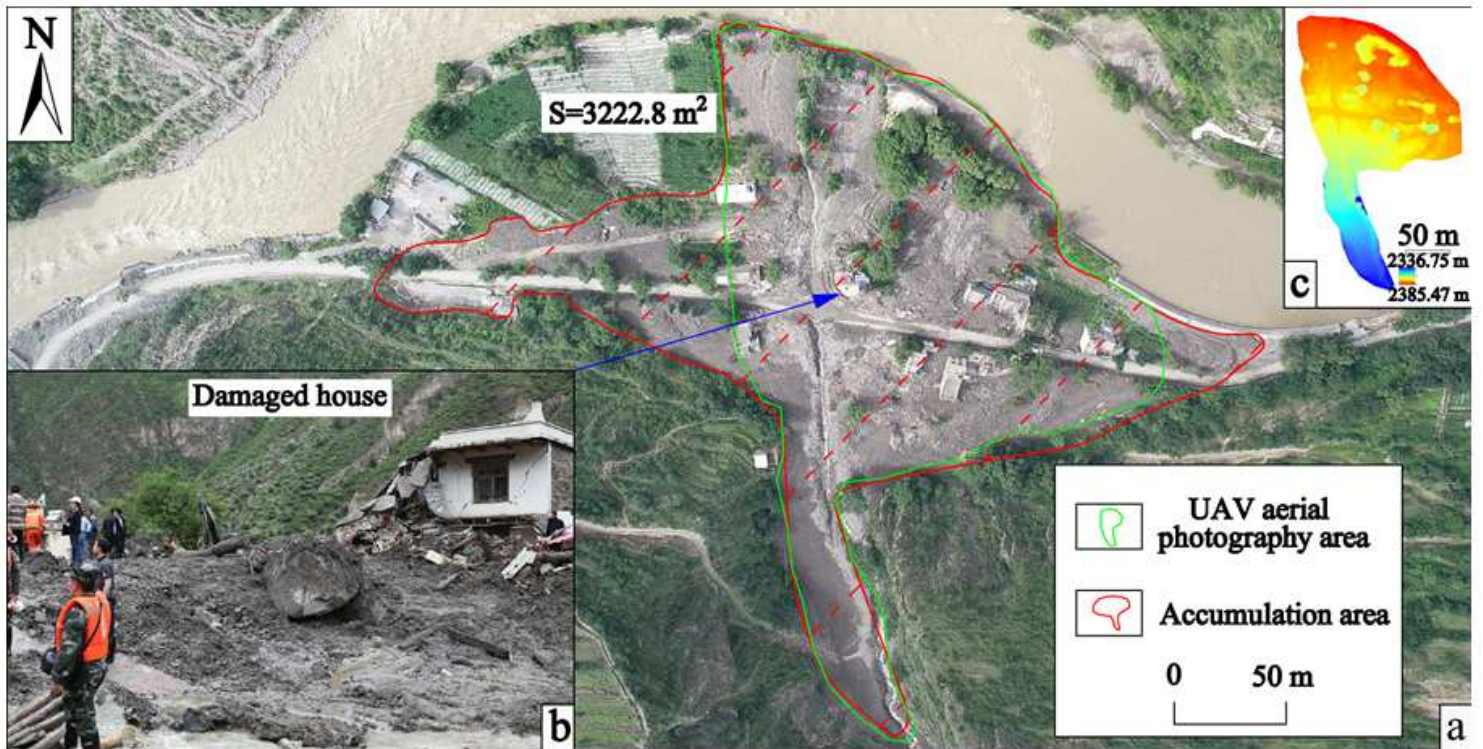


Figure 5

Accumulation area: (a) Accumulation area; (b) Washed-out houses; (c) Altitude image.

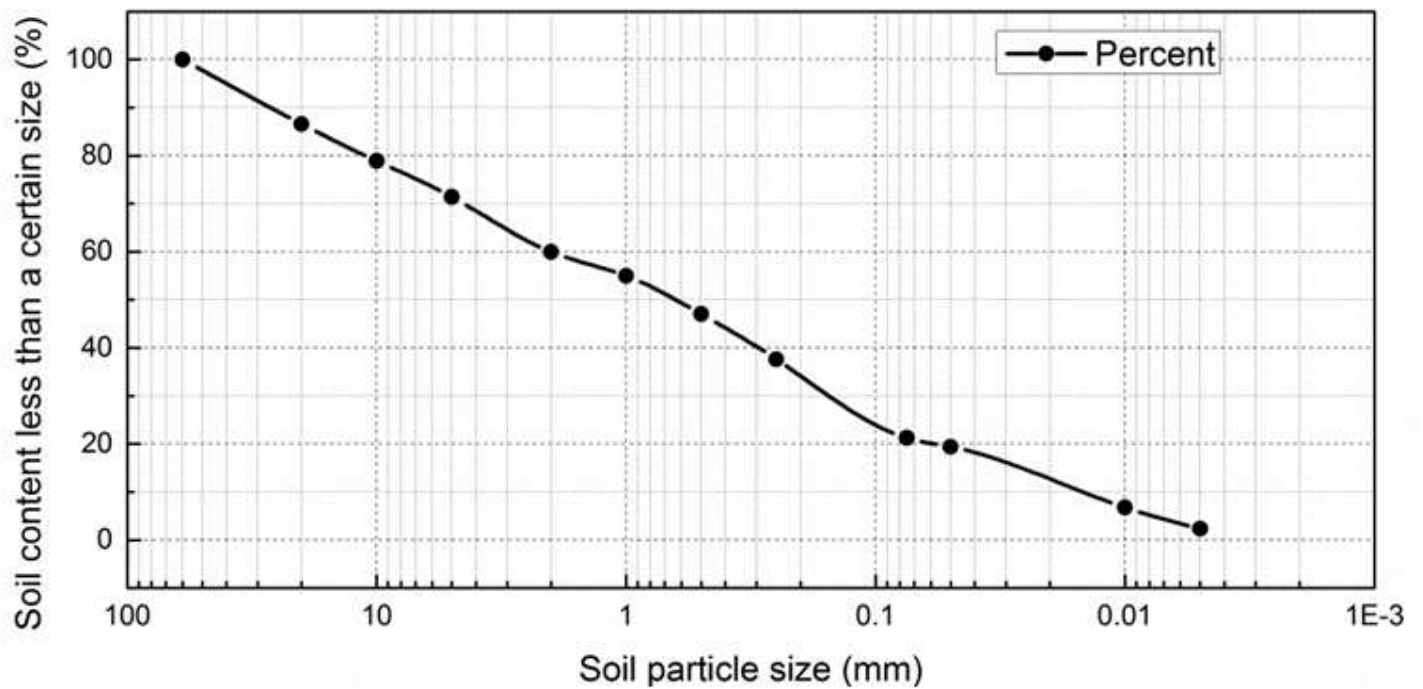


Figure 6

Debris flow accumulation particle curve.

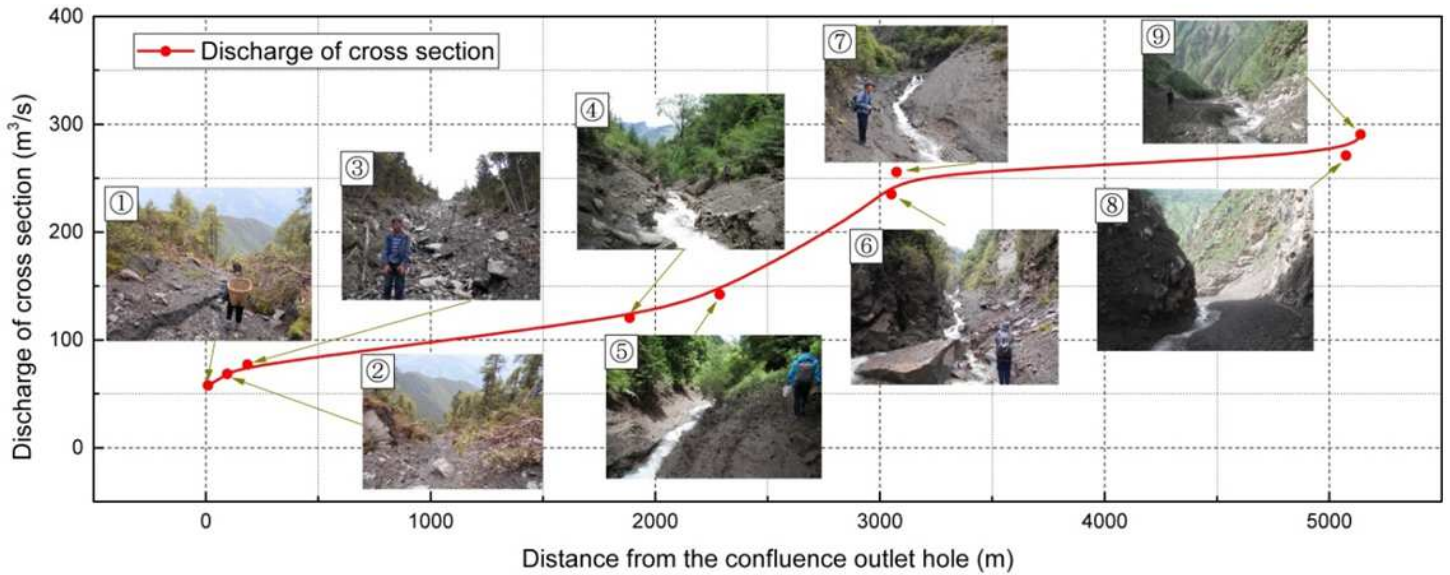


Figure 7

Debris flow discharge process.

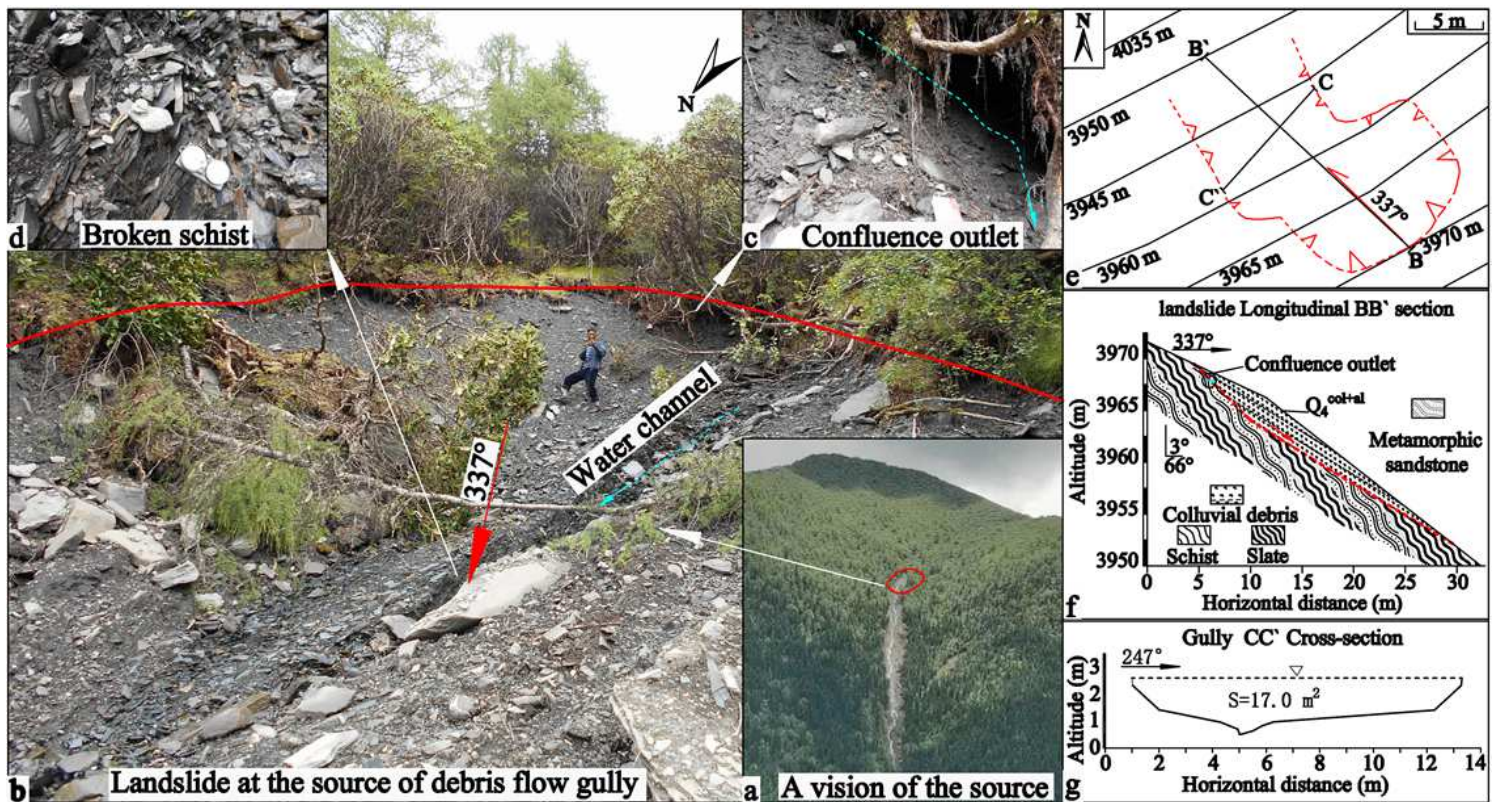


Figure 8

The CDH landslide at the source of the debris-flow gully; (a) The location of the CDH landslide at the source of the gully; (b) The trailing edge of the CDH landslide at the source of the gully and the slide bed; (c) The bedrock on the slide bed; (d) The confluence outlet; (e) Landslide plan; (f) Landslide profile; (g) Landslide cross-section.

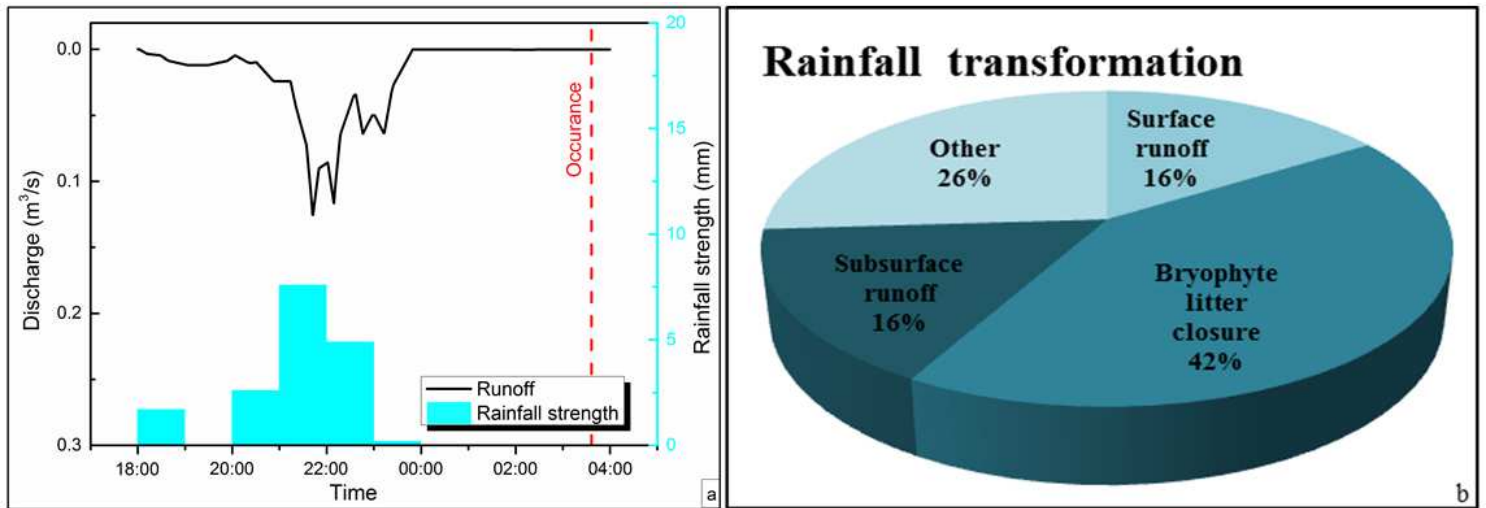


Figure 9

Rainfall and runoff: (a) Runoff process line at the back end of the CDH; (b) Rainfall transformation pie chart.

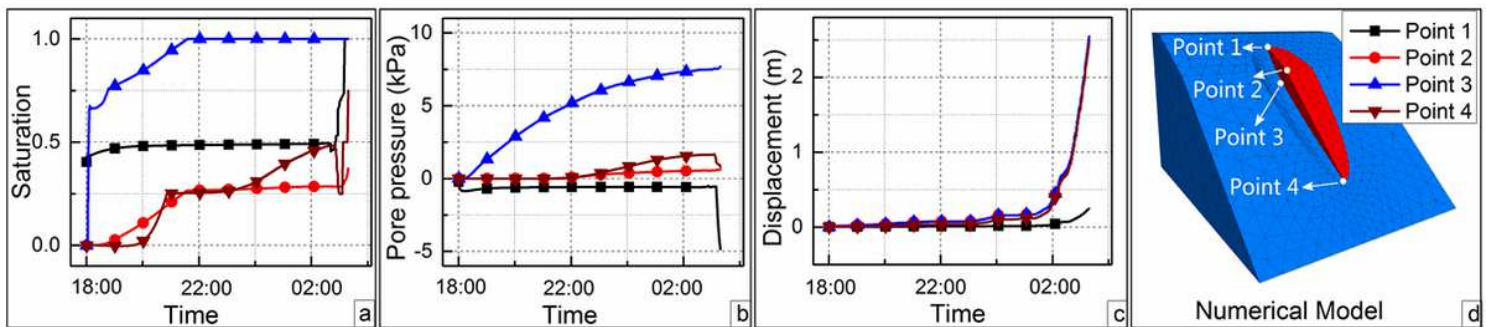


Figure 10

Variation of the CDH parameters at different locations with time: (a) Soil saturation variation curve; (b) Pore water pressure variation curve; (c) Deformation displacement variation curve; (d) Numerical model.

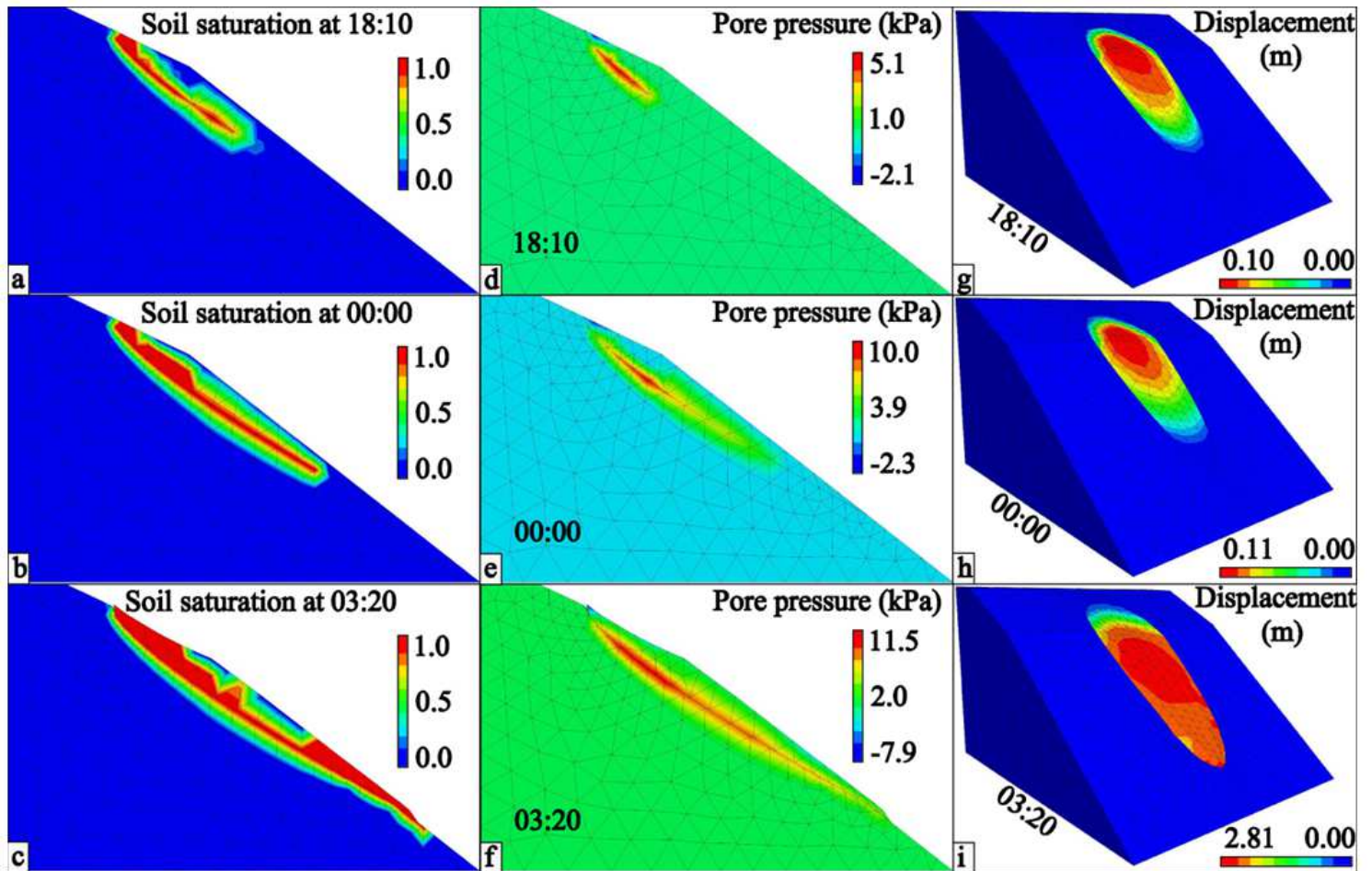


Figure 11

The CDH landslide simulation results: (a) Soil saturation at 18:10 h; (b) Soil saturation at 00:00 h; (c) Soil saturation at 03:20 h; (d) Pore water pressure distribution at 18:10 h; (e) Pore pressure distribution at 00:00 h; (f) Pore pressure distribution at 03:20 h; (g) Total soil deformation at 18:10 h; (h) Total soil deformation at 00:00 h; (i) Total soil deformation at 03:20 h.

Supplementary Files

This is a list of supplementary files associated with this preprint. Click to download.

- [supplyvideo.rar](#)